# QUANTIFYING NON-AXIAL DEFORMATIONS IN RAT MYOCARDIUM

A Thesis

by

KRISTINA DIANE AGHASSIBAKE

Submitted to the Office of Graduate Studies of
Texas A&M University
in partial fulfillment of the requirements for the degree of

MASTER OF SCIENCE

December 2004

Major Subject: Biomedical Engineering

# QUANTIFYING NON-AXIAL DEFORMATIONS IN RAT MYOCARDIUM

A Thesis

by

KRISTINA DIANE AGHASSIBAKE

Submitted to the Office of Graduate Studies of
Texas A&M University
in partial fulfillment of the requirements for the degree of

MASTER OF SCIENCE

Approved as to style and content by:

| | |
|---|---|
| John C. Criscione | Glen Laine |
| (Chair of Committee) | (Member) |
| | |
| Alvin Yeh | William A. Hyman |
| (Member) | (Head of Department) |

December 2004

Major Subject: Biomedical Engineering

# ABSTRACT

Quantifying Non-Axial Deformations in Rat Myocardium.  (December 2004)

Kristina Diane Aghassibake, B.S., Texas A&M University

Chair of Advisory Committee: Dr. John C. Criscione

While it is clear that myocardium responds to mechanical stimuli, it is unknown whether myocytes transduce stress or strain.  It is also unknown whether myofibers maintain lateral connectivity or move freely over one another when myocardium is deformed.  Due to the lack of information about the relationship between macroscopic and cellular deformations, we sought to develop an experimental method to examine myocyte deformations and to determine their degree of affinity.  A set of protocols was established for specimen preparation, image acquisition, and analysis, and two experiments were performed according to these methods.  Results indicate that myocyte deformations are non-affine; therefore, some cellular rearrangement must occur when myocardium is stretched.

*To my family and friends, for all their support and encouragement.*

# ACKNOWLEDGEMENTS

**TABLE OF CONTENTS**

# LIST OF FIGURES

FIGURE                                                                                          Page

**LIST OF TABLES**

**CHAPTER I**

**INTRODUCTION**

Claiming the lives of over 700,000 Americans each year, heart disease has become the single most common cause of death for adults in the United States. According to the American Heart Association (2003), diseases of the heart kill more people than the next five leading causes of death – cancer, chronic lower respiratory diseases, accidents, diabetes mellitus, influenza, and pneumonia – combined. It is estimated that, in the year 2004, the cost of heart disease in the United States will exceed $200 billion, including healthcare expenditures and lost productivity due to morbidity and mortality.

In a diseased heart, myocardium experiences increased hemodynamic loads; consequently, the tissue grows and remodels in a compensatory manner (Emery and Omens, 1997). In some cases, this growth is therapeutic and allows the heart to adapt to abnormal stresses. For example, if stress is applied very gradually to a young, healthy animal, the resulting hypertrophic myocardium expresses normal contractility. However, if the animal is old or unhealthy or if stress is applied rapidly, the result is pathologic hypertrophy in which the tissue expresses decreased contractility. Often, in this case, the hypertrophy is unable to match the inciting stress, cardiac pump function is diminished, and heart failure ensues (Grossman, 1980).

——————

This thesis follows the style and format of Journal of Biomechanics.

While it is clear that myocardium responds to mechanical stimuli, it is unknown whether myocytes transduce stress or strain. It is also unknown whether myofibers maintain lateral connectivity or move freely over one another when myocardium is deformed. Due to the lack of information about the myocardial strain response, the constitutive laws currently in use make assumptions about the behavior of myocardium that have yet to be validated. Hence, we seek to establish more accurate constitutive relations for myocardium and thus improve our experimental models. In order to do so, we must first understand the manner in which myocardial geometry changes in response to deformation, i.e., strain.

The goal of this research project is to develop an experimental method to examine the macroscopic deformations resulting from stretching of myocardium and the corresponding myocyte deformations; it also seeks to quantify the degree to which these deformations are affine. This thesis describes the experimental procedures and protocols for specimen preparation, imaging, and image analysis, and presents the results from two experiments that were performed according to these methods.

**CHAPTER II**

**BACKGROUND**

As early as the seventeenth century, physicians had begun investigating the ultrastructure of muscle tissue. In 1674, Leeuwenhoek observed striations, which he referred to as "spiral bands," in skeletal muscle. In his 1781 Croonian Lecture, John Hunter described his observations of the rearrangement of myofibril components during contraction (Peachey, 1978). More recently, Huxley and Hanson's 1954 essay "Changes in the cross-striations of muscle during contraction and stretch and their structural interpretation" presented their so-called sliding filament theory of muscle contraction, which contains some of the most enduring ideas about the mechanisms of muscle contraction (Huxley and Hanson, 1954).

**CONTRACTILE MECHANISM**

According to Huxley's model, the contractile component of striated muscle consists of interdigitating arrays of thin actin and thick myosin filaments, which overlap in the contractile region (Fig. 1). The overlapping of myofilaments in these arrays results in the repeating band pattern typically observed in striated muscle. The region of overlap between the actin and myosin filaments is known as the A or anisotropic band, while the I or isotropic band contains only actin filaments (Fig. 2). The area that contains only myosin filaments is known as the H zone. Together, the A band, I band, and H zone comprise the sarcomere, the fundamental unit of contraction. The sarcomere

is bounded on both sides by the Z line, which is the structural backbone of the actin

filaments (Opie, 2004).
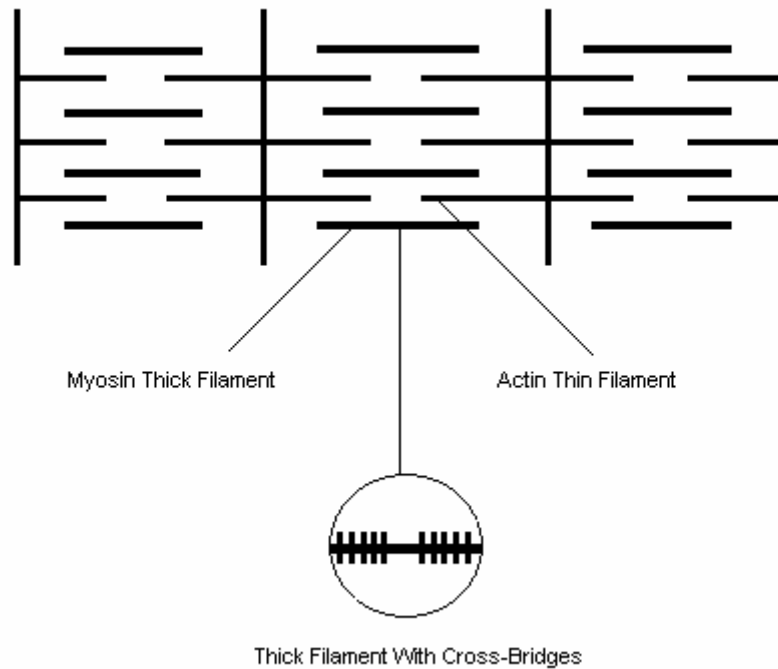


Fig. 1.  Diagram of myofilament arrangement in striated muscle.

In vertebrate striated muscle, the positioning of myofilaments within each array

is very regular; the thick filaments are arranged hexagonally 400 to 450 angstroms apart,

while the thin filaments occupy trigonal positions between the thick filaments (Fig. 2).

The interfilamentous space is filled with sarcoplasm, which is composed primarily of

proteins and other molecules suspended in water (Huxley, 1969).  These myofilament

arrays combine to form myofibrils, which, in turn, make up larger fiber bundles.
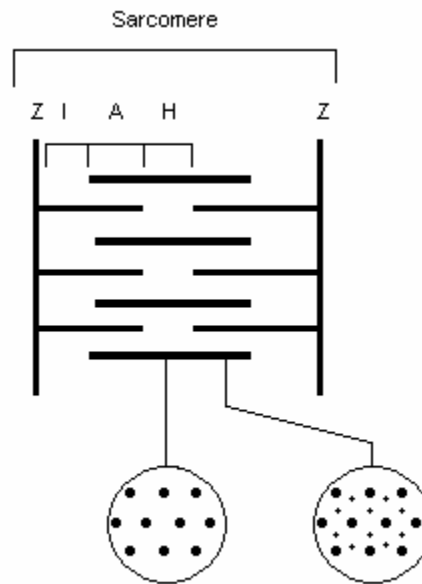
Fig. 2.  Diagram of myofilament lattice in striated muscle.

In Fig. 1, the thick myosin filament is shown enlarged with cross-bridges, irregularly spaced protrusions that Huxley proposed as the sites of mechanical force transmission during contraction.  The interaction between the myosin heads and the actin filaments pulls together the two ends of the sarcomere, causing both filaments to slide without shortening.  This process, known as cross-bridge cycling, is initiated by a wave of electricity passing through the ventricle, which causes an increase in intracellular calcium.  The presence of cytosolic calcium ions allows the myosin heads to bind to the actin filaments, flex, and slide the filaments toward the center of the sarcomere; this flexion shortens the sarcomere and is thought to be the fundamental mechanism of muscle contraction.  Relaxation occurs when, in the presence of ATP, the myosin heads detach from the actin filaments and resume their un-flexed configuration (Opie, 2004).

Nearly forty years after the introduction of the sliding filament theory, Zahalak expanded Huxley's cross-bridge model from a uniaxial description of length changes in the fiber direction to a three-dimensional model that accounts for non-axial active stress (Zahalak, 1996). Zahalak argues that, due to the 180 degree rotation of cardiac muscle fibers from epicardium to endocardium, any ventricular deformation must induce non-axial strains in the majority of fibers in the ventricular free wall.  His theory suggests that, while muscle is generally thought to generate force only in the fiber direction, large cross-fiber deformations may substantially affect both axial and non-axial stresses; he predicts that non-contractile proteins found in the sarcomere play a significant role in this equilibrating effect.

In contrast to earlier studies, Zahalak proposes that altered myofilament spacing due to non-axial strains, rather than changes in ionic concentration, is primarily responsible for the changes in cross-bridge dynamics observed in osmotically perturbed cells.  To support his theory, he cites ionically controlled experiments by Metzger and Moss and Goldman, who observed osmotic influences on both isometric force and maximum shortening speed in skinned skeletal muscle fibers (Metzger and Moss, 1987; Goldman, 1987).  Other studies lend support with findings on osmotic influences on ATP hydrolysis, cross-bridge stiffness, and force generation in intact muscle fibers (Krasner and Maugham, 1984; Goldman and Simmons, 1986; Bagni et al., 1990).

In constructing his model, Zahalak assumes that myofibers do not merely roll over one another "like a stack of greased pencils;" rather, the lateral connectivity of the myofilaments within the muscle fibers prevents simple rearrangement and allows for the

complete transmission of myocardial deformation to the myofibrils themselves (Zahalak et al., 1999). However, in his discussion, Zahalak acknowledges that the actual relationship between macroscopic deformations of myocardium and local deformations of the myofilament lattice has yet to be determined.

Zahalak's simulations of normal myocardium demonstrated that, when non-axial deformations were accounted for, axial active stress was decreased by as much as 35 percent at end-systole. In simulations of compliant, ischemic regions, active stress was decreased by as much as 52 percent; in stiff, infarcted regions, however, the greatest decrease observed was only 29 percent. In all cases, the most significant reductions in end-systolic fiber stresses were predicted at the endocardium, with increasingly larger stresses occurring at the midwall and epicardium. These results, while based on a simplified model of myocardium, suggest that non-axial deformations produce substantial changes in fiber stress and should not be ignored in future models.

**MORPHOLOGY OF VENTRICULAR MYOCARDIUM**

The cells of the atria and the ventricles differ significantly in function and, therefore, in structure. Atrial contraction is responsible for filling the relaxed left ventricle, while ventricular contraction actually propels blood through the vasculature. Because the atria must generate less force than the ventricles, atrial myocytes are smaller and exhibit fewer contractile structures than those in the ventricles (Opie, 2004). For the purposes of this study, our primary interest is the ventricular myocardium.

**Ventricular Myocytes**

The ventricular myocytes are cylindrical in shape and range from 50 – 100 μm in length and from 10-25 μm in diameter. These highly branched cells also possess many transverse tubules (T tubules), invaginations of the sarcolemma which increase the surface area of the cell and assist in the transmission of polarizing electrical signals.

Inside the cell, the contractile apparatus and organelles are not merely suspended in the cytosol as was previously thought. In fact, the sarcoplasm contains a highly structured cytoskeleton, a collection of architectural proteins that serve as scaffolding for the contractile mechanism and connect the cell to extracellular structures. For example, systems of cytoskeletal proteins known as costameres extend from the sarcomere, through the sarcolemma, and attach to the extracellular collagen matrix; these connections allow for bidirectional conduction of mechanical stimuli. Desmin and actin filaments attached to the Z line of each sarcomere allow for the force transmission between sarcomeres that ultimately results in ventricular contraction (Opie, 2004).

Cardiac myocytes are long, multinucleated muscle fibers that are thought to form from the fusion of multiple cells during development. Individual myofibers are bound together by collagen to form muscle fiber bundles, which are arranged such that at any point within the ventricle, there is an appreciable fiber direction. At most points in the normal heart, the fiber direction runs roughly parallel to the epicardial surface; this orientation varies transmurally, from 70° (with respect to the equator) at the endocardium to -60° at the epicardium (Humphrey, 2002).

**Extracellular Matrix**

The connective tissue that encompasses individual cardiac myocytes and holds together the myocardium is known as the extracellular matrix (ECM). Composed primarily of the proteins collagen, fibronectin, and elastin, the ECM contributes to the structural stability of myocardium and is also thought to play a role in certain metabolic processes (Opie, 1998). Fibroblasts, which are responsible for producing most of the fibrous proteins that make up the ECM, are the most plentiful cells in the myocardium, a fact which emphasizes the importance of the ECM. The formation of fibrous myocardial connective tissue, also called fibrosis, is partially regulated by the peptidergic renin-angiotensin-aldosterone system (Opie, 2004).

The helical protein collagen is found in abundance in the ECM and is the primary determinant of myocardial stiffness. Collagen I and collagen III are the two major types of collagen found in myocardium. Collagen I forms thick chains that connect individual myoctes together and conduct mechanical force between the myofilaments and the ECM, while collagen III forms thinner fibers that cross-link with collagen I. Collagen types IV and V are also present in the myocardium, comprising the basement membrane that separates myocytes from their surrounding connective tissue. Collagen fibers also extend from the cytoskeleton to the ECM, attaching the cells to their structural backbone (Opie, 2004). In this manner, cardiac myocytes are held in a fairly ordered configuration; the degree to which individual cells are free to move within this configuration is unknown.

While they were once considered to be passive structural elements of myocardium, Weber has shown that these collagen fibers are degraded and replaced often and therefore play a significant role in growth in remodeling (Weber et al., 1994). In addition, a mechanical model consisting only of coiled collagen fibers proved to be an excellent predictor of stress-strain behavior in canine and rat myocardium; this result indicates that the collagen matrix may in fact be the most important contributor to axial myocardial stiffness (MacKenna et al., 1997). Due to its contribution to muscle stiffness, its ability to prevent myocardial stretch, and its role in cardiac growth, collagen formation in both healthy and diseased tissue is the subject of much investigation.

Elastin, another fibrous extracellular protein, is found wrapped around the collagen matrix and near the sarcolemma. So named because of its rubber-like properties, elastin contributes in part to the ability of myocardium to stretch in response to mechanical factors. Cross-bridge interactions also contribute to myocardial elasticity; the more cross-bridge interactions that occur, the less elastic the myocardium becomes. Also present in the ECM are proteoglycans, such as laminin and fibronectin, which form the underlying mesh on which the collagen matrix is constructed. These proteins also influence cellular growth (Opie, 1998).

According to Smaill and Hunter, Robinson and his colleagues propose other functions for the extracellular connective tissue. The ECM, they argue, serves to limit axial muscle fiber strain, allowing sarcomeres to stretch to lengths of up to 2.25 μm but no further. They attribute this "strain-locking" mechanism to a rearrangement of connective tissue that occurs upon stretching the myocardium and increases stiffness

(Smaill and Hunter, 1991). The fact that sarcomere lengths increase when the collagen matrix is destroyed supports this theory (MacKenna et al., 1994). Robinson also suggests that, during myocardial contraction, the ECM might store energy to be utilized for the rapid expansion that accompanies ventricular filling (Robinson et al., 1986).

**Laminar Myofiber Architecture**

In addition to supporting and connecting myocytes, the extracellular collagen matrix arranges bundles of cells into sheets, or laminae; these laminae are, on average, three to four cells thick and exhibit multiple branches (Fig. 3).
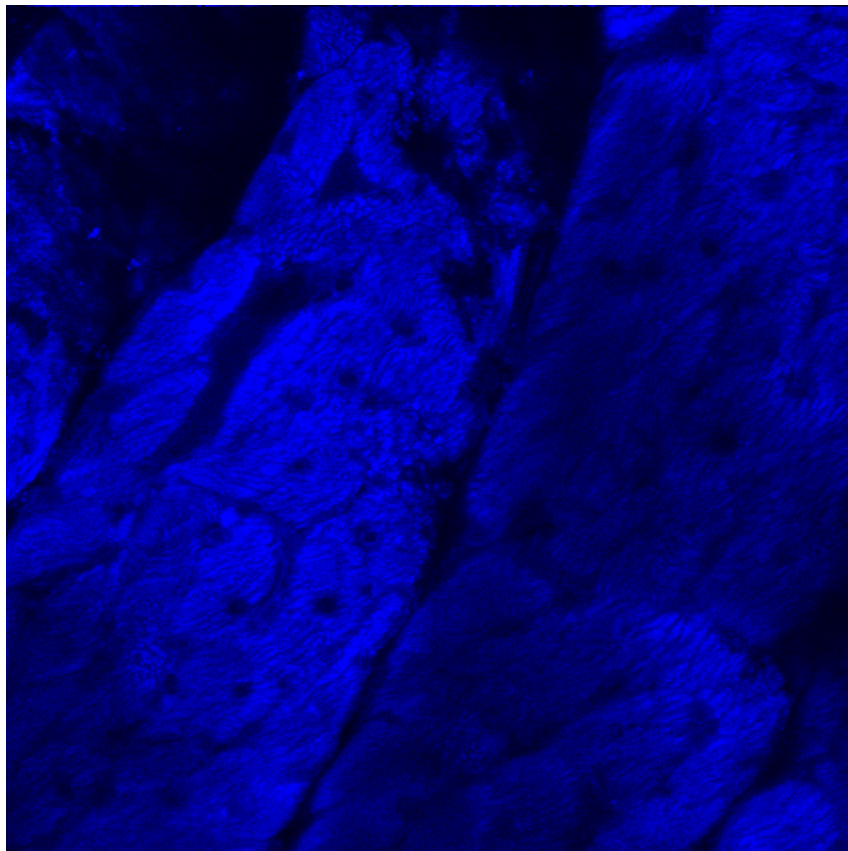


Fig. 3. Multiphoton micrograph of rat myocardium showing myocytes
organized into visible laminae (60x).

Similar to the helical arrangement of myofibers, myocardial laminar orientation varies transmurally; LeGrice and colleagues showed that, in tangential section, the layers of myocardium run approximately parallel to the local fiber direction (LeGrice et al., 1995).  In the right and left ventricle free walls, laminar orientation changes from -90° at the endocardium to 30-60° at the epicardium (Fig. 4a).  In the interventricular septum, however, the orientation changes a full 180° such that the laminae run longitudinally at both the right and left ventricle subendocardia (Fig. 4b).



Epicardium                    Midwall                    Endocardium
30-60°                          0°                          -90°
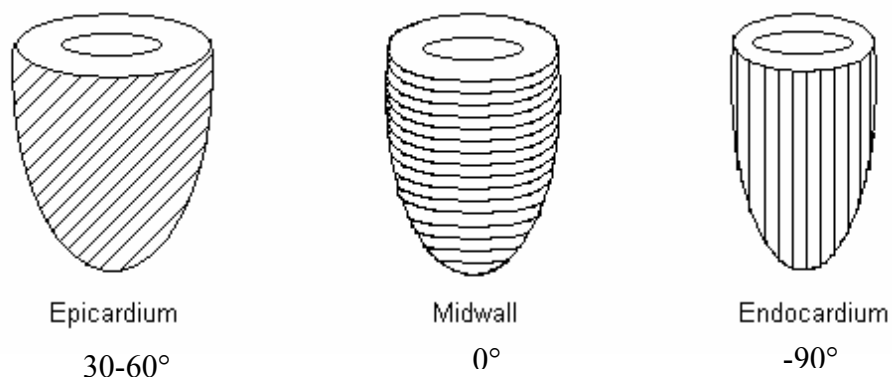
Fig. 4a.  Laminar orientation in right and left ventricular myocardium.



LV Subendocardium        Midwall        RV Subendocardium

90°                          0°                          -90°
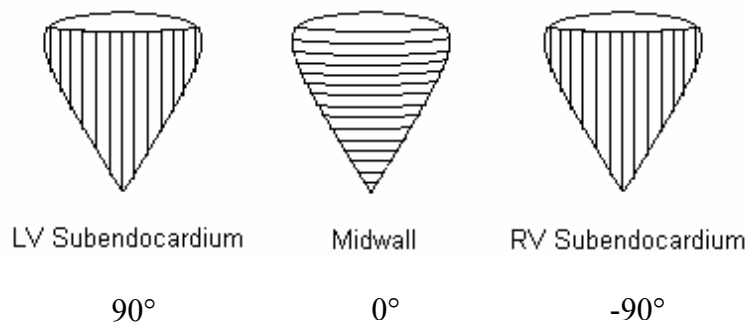
Fig. 4b.  Laminar orientation in the interventricular septum.

Separating the laminae from one another are long collagen fibers that are attached to the connective tissue matrix. While these fibers do link adjacent layers of myocardium, they also create distinct cleavage planes along which laminar slippage is thought to occur. Also connecting adjacent laminae are sparse branches one to two cells thick. The distribution of these cellular branches varies transmurally, with a minimum average branching density of 3.8 branches/mm$^2$ at the midwall and higher branching densities of 6.6-8.4 branches/mm$^2$ near the endocardium and epicardium. The spacing of branches along a sheet of myocardium is quite irregular, and the distance between consecutive branches can be as much as 1-2 mm. The local distribution of branches appears to be unrelated to the amount of extracellular space between adjacent laminae (LeGrice et al., 1995).

While its exact role is not well understood, the laminar fiber architecture of myocardium is thought to contribute substantially to ventricular function. In systole, the left ventricle free wall and interventricular septum thicken as sheets of myocardium extend and shear; the opposite occurs during diastole. The extent to which each of these mechanisms – sheet shear and sheet extension – is responsible for wall thickening varies regionally and transmurally. In addition, the degree of laminar reorientation is load-dependent, with increased rearrangement observed in response to increased end-diastolic pressure (Takayama et al., 2002). Based on their examination of the effects of fiber shortening and laminar reorientation on ventricular systolic strain, Costa and colleagues suggest that myocytes may also rearrange within the laminae to produce the ventricular wall thickening that is observed at end systole (Costa et al., 1999).

**MODELING VENTRICULAR MYOCARDIUM**

In cardiac mechanics, we typically view myocardium as a material continuum, and we therefore employ a continuum mechanics approach in our analyses of stress, strain, and other mechanical characteristics. Classically, a material continuum defines a relationship between material particles such that between any two particles lies another particle, and each particle within the continuum has mass. In a biological system, however, it is clear that the scale at which we consider a material is critical to the continuum approach. At the atomic level, for example, the motion and interaction of particles cannot be described by Newtonian mechanics, and the vast amount of empty space between particles makes continuum mechanics inappropriate for atomic investigation. Yet, if we choose to consider very large collections of atoms, such as a group of cells, the continuum mechanics approach is fitting (Fung, 1993). While it is true that there is space between the cells of the myocardium, the amount of space is small in relation to the particle size (i.e., the size of the cell); hence, this simplification results in only small errors but greatly facilitates mechanical analysis.

Adopting the continuum approach, a model of cardiac mechanics consists of the following components: kinematics, applied and body forces, boundary conditions for pressure and displacement, balance relations for mass, momentum, and energy, and constitutive relations describing the material behavior of ventricular myocardium (Humphrey, 2002).

**General Characteristics of Ventricular Myocardium**

As previously discussed, myofiber orientation, laminar architecture, and the extracellular collagen matrix all contribute to the underlying mechanism of ventricular contraction. These elements are also responsible for the material symmetry observed in ventricular myocardium. Inspection of muscle fiber orientation, for example, suggests transverse isotropy, while the laminar fiber organization suggests orthotropy; elements of the ECM contribute to both types of symmetry (Humphrey, 2002). Nevertheless, for convenience, most models of myocardium assume that the tissue behaves isotropically in the plane perpendicular to the muscle fiber direction. In addition, the composite nature of myocardium leads to regional differences in response to mechanical stimulus.

The response of myocardium to stress and strain is not unlike that of other soft tissues. In general, the mechanical behavior of soft tissue is said to be viscoelastic, that is, the tissue exhibits stress relaxation, creep, and hysteresis. Stress relaxation occurs when a body subject to constant strain experiences a corresponding stress that decreases with time. When a body is subjected to a sudden stress, the body deforms (strains) accordingly; if the stress is held constant but the body continues to deform, it is said to exhibit creep. Often, under cyclic loading, the stress-strain relationship of the tissue differs during loading and unloading, a phenomenon known as hysteresis. Ventricular myocardium demonstrates all three of these characteristics, and is therefore a viscoelastic material. However, in the case of cyclic loading, myocardium behaves elastically when the loading and unloading phases are considered independently; hence,

many investigators choose to treat myocardium as a pseudoelastic material, a convenient simplification (Fung, 1993).

Also critical to myocardial constitutive relations is residual stress, the stress present in an unloaded body. While its exact source is unknown, residual stress is thought to originate from growth and remodeling, and it has been shown to change when pathologic or adaptive growth occurs (Costa et al., 2001b). These stresses, also known as body stresses, are accompanied by residual strains of 4-7% (Costa et al., 1997). Because they ensure that myocardium is never really "stress-free," residual stresses must be considered when developing constitutive relations and models for both active and passive (i.e., non-contracting) myocardium.

**Theoretical Framework**

While it is possible to obtain descriptors of material behavior from experimental data or by trial and error, Humphrey (2002) contends that constitutive relations should be theoretically derived. Theoretical formulations, he argues, are superior because they are based on the microstructure, which ultimately determines the observed material behaviors. However, difficulty in mathematically describing the constituents and their interactions often precludes investigators from adopting this approach. Clearly, more information about the nature of the microstructural response of myocardium would facilitate the development of better constitutive relations; this study seeks to provide exactly this kind of information.

Humphrey discusses a landmark study which established that constitutive relations for rubber-like materials could be formulated based directly on information

gleaned from in-plane biaxial testing on thin, rectangular specimens; this result led many investigators to develop protocols for biaxial testing on myocardium. For demonstration, we will consider two theoretically derived models of myocardium: one which aims to determine a strain-energy function for biaxially stretched passive myocardium, another which describes active stress in contracting cardiac myofibers.

*Modeling Passive Myocardium*

While it remains the simplest and most common method of material testing, the uniaxial extension test provides only one-dimensional view of myocardium. Because myocardium deforms three-dimensionally in vivo, three-dimensional testing would yield the most complete results. However, due to technical limitations, biaxial testing is often used to gain valuable insight into the myocardial stress-strain response (Costa et al., 2001a).

Humphrey et al. (1990) established a theoretical framework for biaxial tests on passive myocardium based on myocardial histology and assumptions of transverse isotropy, incompressibility, local homogeneity, and pseudoelasticity. Humphrey and colleagues seek to develop a strain-energy function based on invariants $I_1$ and $I_4$, where

$$I_1 = tr\mathbf{C} = tr\mathbf{B} \tag{1a}$$

$$I_4 = \mathbf{N} \bullet \mathbf{C} \bullet \mathbf{N} \tag{1b}$$

and **B** and **C** are the left and right Cauchy-Green deformation tensors and **N** is "a unit normal vector defining the preferred direction of the material in the undeformed configuration" (Humphrey, 1990). Note that, for the deformation gradient **F**, $\mathbf{C} = \mathbf{F}^T \bullet \mathbf{F}$ and $\mathbf{B} = \mathbf{F} \bullet \mathbf{F}^T$. The strain-energy function, then, is defined as

$$W = W(I_1, I_4) \tag{2a}$$

or, because, $I_4 = \alpha^2$, where $\alpha$ is the axial stretch ratio,

$$W = W(I_1, \alpha). \tag{2b}$$

For a material described by W, the Cauchy stress is

$$\mathbf{t} = -p\mathbf{I} + 2W_1\mathbf{B} + (W_\alpha/\alpha)\mathbf{F} \bullet \mathbf{N} \otimes \mathbf{N} \bullet \mathbf{F}^T \tag{3}$$

where $p$ is a Lagrange multiplier, $\mathbf{I}$ is the identity tensor, $W_1 = \partial W/\partial I_1$, and $W_\alpha = \partial W/\partial \alpha$.

Following their theoretical formulations, Humphrey and colleagues performed biaxial tests on six samples of excised canine myocardium. Based on their observations that

(i) $W_1$ and $I_1$ are (almost) linearly related

(ii) $W_1$ and $\alpha$ are (almost) inversely related

(iii) $W_\alpha$ and $\alpha$ are nonlinearly, but not exponentially, related

(iv) $W_\alpha$ and $I_1$ are (almost) inversely related,

they propose the following form of the pseudo-strain energy function to describe passive myocardium:

$$W(I_1, \alpha) = W(I_1, \alpha) \sum_{i=0}^{n} \sum_{j=0}^{n} c_{ij}(I_1 - 3)^i (\alpha - 1)^j \tag{4}$$

where $c_{ij}$ are material parameters. Setting $n = 3$, expanding (4), and enforcing the aforementioned observations yields

$$W = c_1(\alpha - 1)^2 + c_2(\alpha - 1)^3 + c_3(I_1 - 3) + c_4(I_1 - 3)(\alpha - 1) + c_5(I_1 - 3)^2. \tag{5}$$

This pseudo-strain energy function was the first of its kind, i.e., the first descriptor of the mechanical behavior of myocardium based on information gleaned from rigorous biaxial testing.  Subsequent studies provided more information about myocardial stiffness and transmural variations in material parameters.  For example, ventricular myocardium was observed to be up to three times stiffer in the fiber direction than in the cross-fiber direction (Costa et al., 2001a).  This result suggests that myofibers may be only loosely bound laterally and thus could potentially experience some degree of translational motion upon ventricular deformation; the possibility of this type of motion is under investigation in the current study.

Biaxial tests and theoretical formulations allow for the development of increasingly descriptive constitutive relations and, consequently, increasingly sophisticated models of the mechanical behavior of myocardium.  However, this type of analysis does have limitations, namely the exclusion of shear deformations from testing protocols and the use of thin samples of myocardium, the material properties of which may not be representative of intact tissue (Costa et al., 2001a).

*Modeling Active Myocardium*

Because myocardium is a contractile tissue, it is highly unlikely that a single constitutive law based on passive material properties can accurately describe its mechanical behavior throughout the cardiac cycle.  A complete constitutive law would account for both the passive and active properties of myocardium, but due to experimental difficulties, there is currently a lack of information available about the fundamental nature of contracting myocardium.

Like passive myocardium, active myocardium is most often modeled one-dimensionally, and these models consider only axial fiber stress and force generation. However, in biaxial tests on barium-contracted excised rabbit myocardium, Lin and Yin (1998) measured significant cross-fiber stresses, which were on average 46% of the axial fiber stresses observed in their seven specimens. Based on these results, it is apparent that future models of active myocardium must incorporate non-axial components of mechanical parameters. One such model developed by Zahalak (1996, 1999) was discussed previously and suggests that axial fiber stresses are greatly affected by non-axial muscle fiber deformations. However, Zahalak's model maked assumptions about myocardial geometry that have yet to be validated, and he highlighted the need for more investigation in this area.

**GROWTH AND REMODELING**

During development and disease, the heart grows and remodels in response to increased hemodynamic loads and this growth often involves changes in the morphology of ventricular myocardium. In particular, disease has been shown to alter wall thickness, myocyte size, and muscle fiber orientation. It is likely that myocardial growth is regulated, at least in part, at the cellular level by mechanical factors such as stress and strain, but it is unknown whether myocytes themselves are capable of transducing mechanical stimuli (Omens, 1998). Whatever the inciting stimulus, myocardial remodeling probably occurs in a compensatory manner that returns the stimulus to a normal level (Emery and Omens, 1997).

Muscle fiber orientation is critical to ventricular contraction as it contributes to ventricular torsion and wall thickening. Even in the developing fetus, the heart exhibits a complex myofiber arrangement (McLean et al., 1989). It comes as no surprise, then, that disruptions of the myofiber architecture substantially alter ventricular mechanics. In a study of transgenic mice, Karlon et al. (2000) found that myofiber disarray is associated with reduced septal torsion and reduced systolic shortening on the septal surface. Altered myofiber orientation has also been observed in pressure overload hypertrophied canine hearts (Carew and Covell, 1979). These results and the fact that myofiber disarray is observed in certain diseases of the human heart underscore the fact that myofiber arrangement is a substantial contributor to cardiac mechanics.

Another change in ventricular morphology that occurs during myocardial growth and remodeling is increased cellular size. Myocyte cross-sectional area has been shown to increase as a result of pressure overload hypertrophy (Omens et al., 1996), while ischemic and dilated cardiomyoapathies are characterized by increased myocyte length (Gerdes and Capasso, 1995). Because disease clearly alters myocardial geometry, this study considers only normal, healthy, adult myocardium.

CHAPTER III

METHODS


**ANIMAL MODEL**

Two male Sprague-Dawley rats were housed at the Laboratory Animal

Resources and Research facility at Texas A&M University for use in this experiment.

The animals were used in accordance with the Public Health Service's *Guide to the Care*

*and Use of Laboratory Animals.* The adult rats underwent nonsurvival thoracotomies,

which were performed by Dr. John C. Criscione. Hearts were arrested by cold

cardioplegia, harvested, immediately submerged in potassium phosphate buffered saline,

and transported.

**SPECIMEN PREPARATION**

Each animal was weighed, sacrificed by $CO_2$ asphyxiation, and placed in the

supine position. Using scissors, a transverse incision was made distal to the xiphoid

process; a second transverse incision was made through the diaphragm, resulting in

bilateral pneumothorax. A midline incision was then made from the distal aspect of the

sternum to the clavicle, severing the rib cage and exposing the thoracic cavity.

Approximately 5 ml of cold .02 M potassium phosphate buffered saline were injected

into the apex of the heart to perfuse the tissue and arrest contraction of the myocardium.

The inflow and outflow tracts were cut, allowing the heart to be removed from the

thoracic cavity and submerged in potassium phosphate buffered saline. The harvested

tissue was then transported to the Cardiovascular Mechanics Research Group Laboratory.

Once in the laboratory, each heart was weighed and dissected to isolate the interventricular septum. Using the conus arteriosus as a guide, a vertical incision was made down the right ventricle free wall. The right ventricle was opened to expose the papillary muscles, which were severed. Vertical incisions were made along the anterior and posterior interventricular sulci to remove the two segments of right ventricle free wall. The left ventricle free wall was removed in a similar fashion; a vertical incision allowed for opening of the left ventricle, severing of the papillary muscles, and removal of the anterior and posterior segments of the left ventricle free wall. Once isolated, a final vertical incision separated the septum into anterior and posterior segments. The two segments of the septum were then photographed alongside a metric length scale using a Kodak Easy Share DX4900 Zoom digital camera (Eastman Kodak Company, Rochester, NY) (Fig. 5a, b); these digital photos were later used to precisely determine pre-fixation reference lengths for the anterior and posterior segments of the septum.
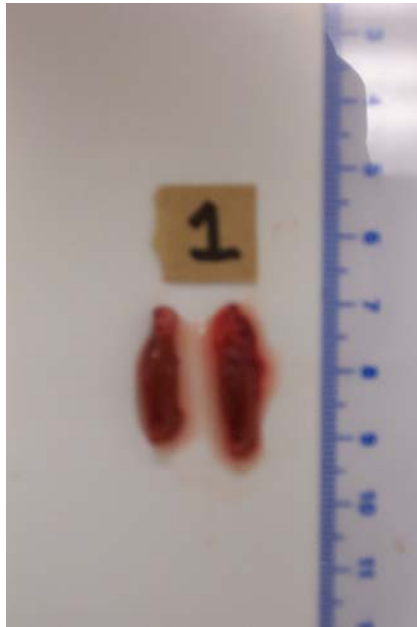
Fig. 5a. Unstretched segments of septum alongside metric length scale (Animal 1).



Fig. 5b. Unstretched segments of septum alongside metric length scale (Animal 2).

**EXPERIMENTAL PROTOCOLS**

For each animal, one segment of the septum was stretched before formalin
fixation, while the other segment was fixed unstretched.  Using 4-0 silk suture, a
modified mattress stitch was made near the proximal aspect of the anterior segment of
the septum and tied to point A on the stretching device; similarly, the distal aspect of the
anterior segment of the septum was tied to point B on the stretching device (Fig. 6).
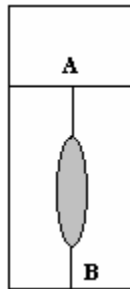
Fig. 6. Anterior segment of septum attached to stretching device.

The posterior segment of the septum was sutured in a similar fashion but was not tied to
a stretching device, creating visual reference points on the posterior segment (Fig. 7a,b).

Fig. 7a. Stretched and unstretched segments of septum prior to fixation (Animal 1).
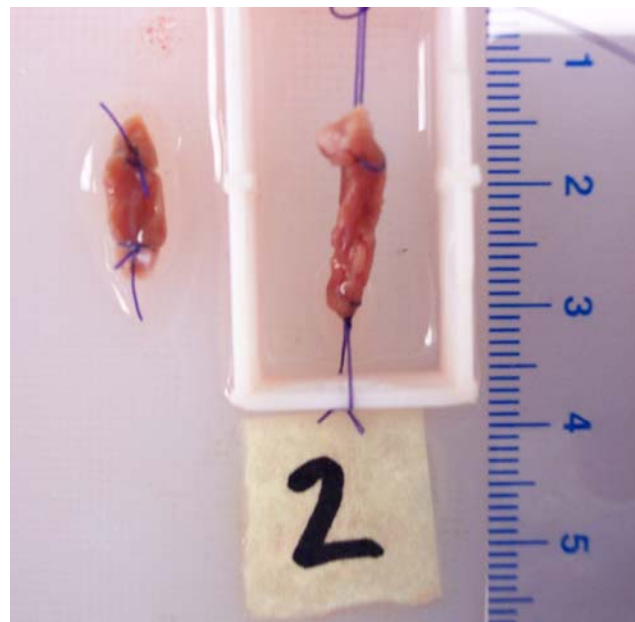


Fig. 7b. Stretched and unstretched segments of septum prior to fixation (Animal 2).

The anterior segment was submerged in formalin while still attached to the stretching device; the posterior segment was also submerged in formalin.  Both segments of the septum were kept refrigerated in formalin to allow infiltration and fixation of the tissue.  Specimens from the animals were used according to the schedule outlined in Table 1.

Table 1. Schedule of stretching for anterior and posterior segments of septum.

| Animal | Stretched Segment | Unstretched Segment |
|--------|-------------------|---------------------|
| 1 | Anterior | Posterior |
| 2 | Posterior | Anterior |

Following fixation, the tissue was removed from formalin and photographed a third time alongside a metric length scale using the same digital camera (Fig. 8a, b).

Fig. 8a. Segments of septum following fixation,
with anterior segment sutured to stretching device (Animal 1).



Fig. 8b. Segments of septum following fixation,
with posterior segment sutured to stretching device (Animal 2).

The stretched segment was cut free from the stretching device and both segments of the septum were blotted dry and photographed a fourth time (Fig. 9a, b).  The tissue was then submerged in formalin once again and transported to the Image Analysis Laboratory at the College of Veterinary Medicine.
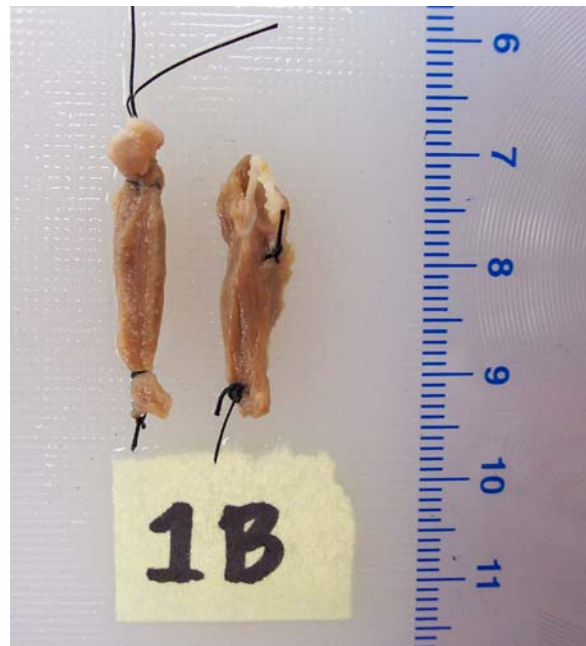


Fig. 9a. Stretched and unstretched segments of septum following fixation,
with anterior segment cut free from stretching device (Animal 1).

Fig. 9b. Stretched and unstretched segments of septum following fixation,
with posterior segment cut free from stretching device (Animal 2).

**IMAGE ACQUISITION**

In order to determine the best imaging method for this project, several techniques were tried using excess tissue.  Originally, we planned to obtain images from thin sections of tissue using light microscopy and sought only to select an embedding medium.  First, a sample was dehydrated in graded ethanols, cleared in Histoclear (National Diagnostics, Atlanta, GA), and embedded in Paraplast tissue embedding medium (Tyco Healthcare/Kendall, Mansfield, MA).  The embedded sample was then sectioned, with much difficulty, using a microtome.  Due to the tissue distortion that occurred upon dehydration and the inability to obtain useful sections, this method was found to be unsuitable.  In order to avoid the dehydration process and the consequent tissue distortion, other samples were embedded in JB-4 plastic (Polysciences,

Warrington, PA) and sectioned.  Though the plastic embedding medium was better

suited to the project than paraffin, we were still unable to section the samples to our

satisfaction.  As a result, we opted to circumvent the issue of sectioning our tissue

samples altogether and chose instead to employ multiphoton microscopy, which does not

require that specimens be thinly sectioned.

  Imaging was performed at the Image Analysis Laboratory under the supervision

of Dr. Alvin Yeh and Dr. Roula Mouneimne.  Specimens were examined using a Bio-

Rad Radiance 2000 MP multiphoton microscope (Bio-Rad Laboratories, Hercules, CA),

using a Tsunami mode-locked Ti:sapphire laser (Spectra-Physics, Mountain View, CA)

tuned to 840 nm.  Micrographs were captured using the Bio-Rad LaserSharp software

that complements the Radiance 2000 MP system.

**CHAPTER IV**

**RESULTS**

Data were collected for two animals.  The animals were determined to be

healthy, adult specimens by comparison of their heart and total body weights with

established standards (Table 2).  When evaluating the data, only images that contained

10 or more distinguishable cells were analyzed.

Table 2. Comparison of heart weights of Animals 1 and 2 with standard for healthy, adult, male Sprague-Dawley rats (Taconic Technical Library, 2002).  *Heart weights expressed as percent of total body weight.

| Model | Heart Weight* |
|---|---|
| Standard | 0.29-0.54 |
| Animal 1 | 0.29 |
| Animal 2 | 0.30 |

**IMAGE ANALYSIS**

Image analysis was performed using Matlab; the annotated code is available in

Appendix A.  The raw images were converted from tagged image file format (TIFF) to

bitmap format in Microsoft Photo Editor and were then imported into Matlab.  Using a

cursor, points on the boundary of each cell were individually selected (Fig. 10) and the

corresponding pixel values were used to plot the cell's boundary (Fig. 11), interior, and

centroid (Fig. 12).  All cells whose boundaries were clearly visible were selected; no

preference was given to cells that appeared to be more circular in cross-section. When boundaries between cells were unclear, the entire region in question was considered to be one "cell group," and points were selected on the group's boundary. In addition, as shown in Fig. 10, the centroids from previously selected cells on each micrograph were plotted to ensure that cell data was not duplicated. Each micrograph used to obtain cell data is available in Appendix B; the centroids of selected cells are shown on these images.
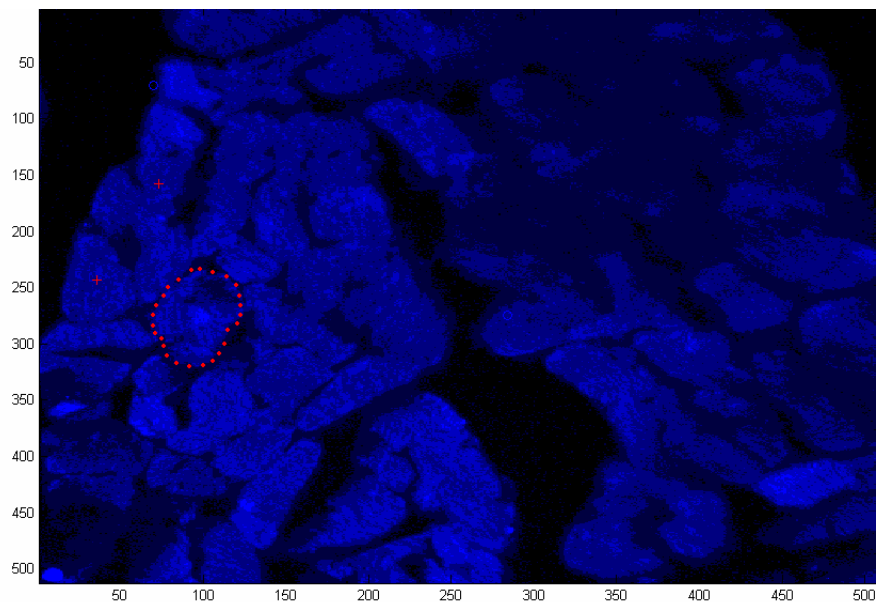


Fig 10. Matlab figure showing points selected on cell boundary and centroids of previously selected cells.
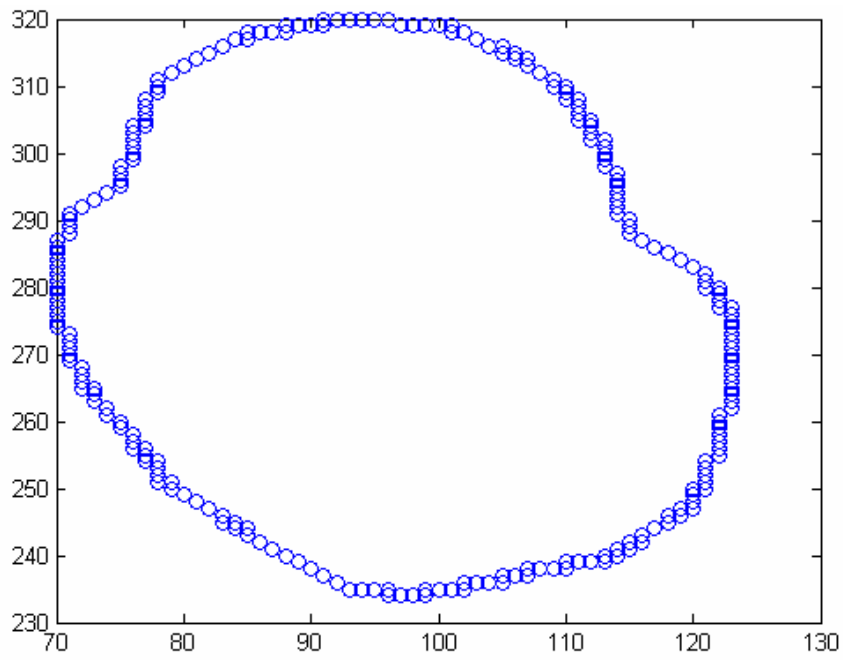
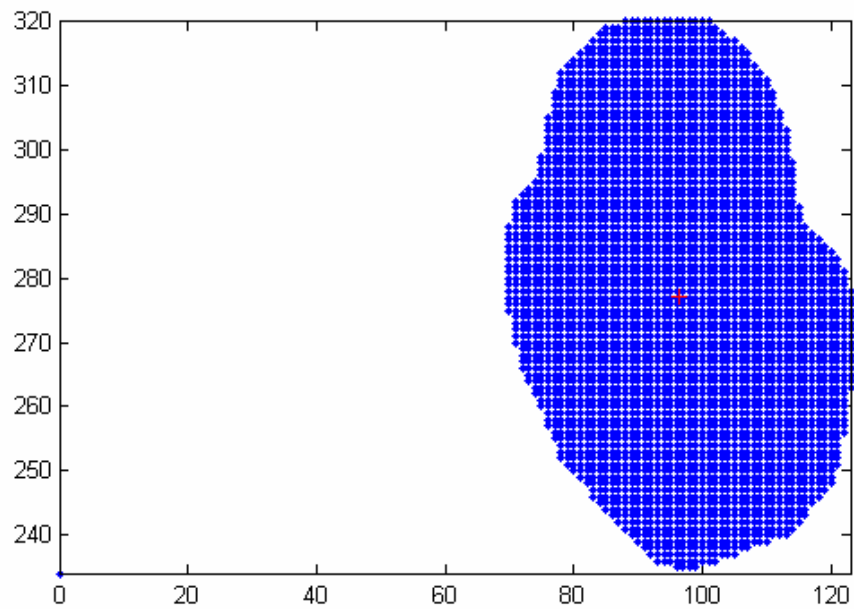Fig. 11. Plot of cell boundary generated from selected points.



Fig. 12. Plot of cell interior and centroid generated from selected points.

For each unsretched cell, we then calculated the second moments of area about the centroid, which are given by

$$I_x = \iint x^2 \, dA \tag{6a}$$

$$I_y = \iint y^2 \, dA \tag{6b}$$

For our purposes, we computed the moments by summation and considered their square roots:

$$\sqrt{I_x} = \sqrt{\frac{\sum x^2}{A}} \tag{7a}$$

$$\sqrt{I_y} = \sqrt{\frac{\sum y^2}{A}} \tag{7b}$$

where A is the cell area in pixels and x and y represent the distance from a point P in the interior of the cell to the cell's centroid in the x- and y-directions, respectively (Fig. 13). The ratio of square roots of the moments for unstretched cells, $\rho_{undeformed}$, was determined by

$$\rho_{undeformed} = \frac{\sqrt{I_x}}{\sqrt{I_y}} \tag{8}$$

We also calculated what this ratio would be for the selected myocytes if they deformed with complete affinity:

$$\rho_{affine} = \lambda^2 \frac{\sqrt{I_x}}{\sqrt{I_y}} \tag{9}$$

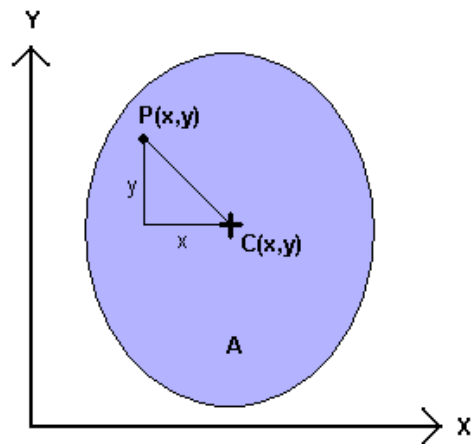where $\lambda$ is the stretch ratio measured for the specimen of interest.

Fig. 13. Diagram of cell showing X- and Y-coordinate axes, interior point P, and centroid C.

In the stretched images, the actual direction of stretch was unknown and it was necessary to perform a transformation of coordinates before calculating ρ.  In order to do so, we determined the major and minor axes of each cell and found the orientation angle, α, between the minor and x-axes (Fig. 14).
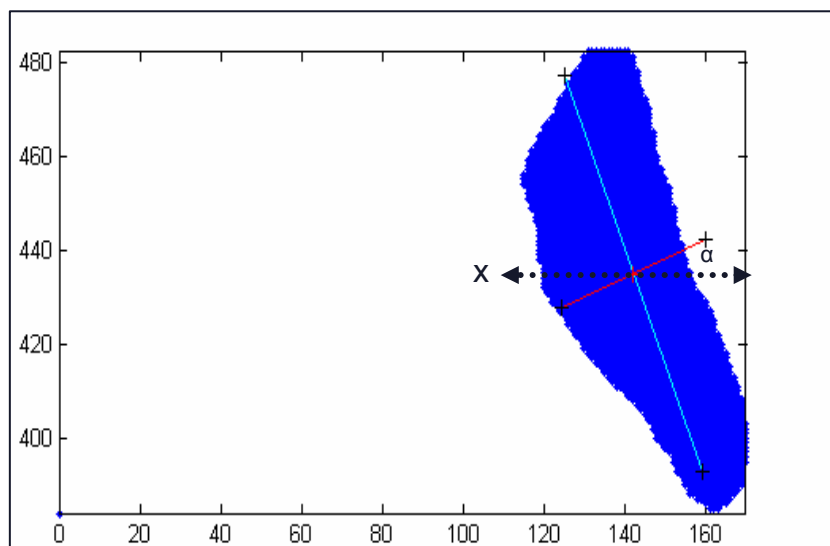


Fig. 14. Stretched cell plotted with major, minor, and x-axes and orientation angle α.

We determined an average $\alpha$ for each image and assumed the stretch direction to be defined by $\alpha + \pi/2$. $I_x$ and $I_y$ were found by

$$I_x = I_{x'}^2 \cos^2 \alpha_{avg} + I_{y'}^2 \sin^2 \alpha_{avg} - 2I_{x'y} \sin \alpha_{avg} \cos \alpha_{avg} \qquad (10a)$$

$$I_y = I_{x'}^2 \sin^2 \alpha_{avg} + I_{y'}^2 \cos^2 \alpha_{avg} + 2I_{x'y'} \sin \alpha_{avg} \cos \alpha_{avg} \qquad (10b)$$

where x' and y' refer to an orthogonal coordinate system defined by the cell's major and minor axes and $I_{x'y'}$ is the area product of inertia:

$$I_{x'y'} = \frac{\sum x'y'}{A} \qquad (11)$$

A second Matlab code was written to quantify the macroscopic deformations that resulted from stretching the tissue samples (Appendix A). Using photographs of the samples before and after stretching and fixation (see Fig. 7, 9) and the metric length scales they contain, stretch ratios were calculated for each sample as follows:

$$\lambda = \frac{L}{L_O} \qquad (12)$$

where $\lambda$ is the stretch ratio, $L_0$ is the length of the fresh sample prior to stretching and fixation, and L is the length of the sample following stretching, fixation, and removal from the stretching device. The photographs used to determine the stretch ratios of the specimens can be found in Appendix C; these images show the marker points that were used for measurement of L and $L_0$.

**MACROSCOPIC DEFORMATIONS**

Stretch ratios were determined for both the stretched and unstretched segments of the septum. These ratios are summarized in Table 3, where $\lambda_{1U}$ denotes the stretch ratio

for the unstretched segment from Animal 1, $\lambda_{1S}$ denotes the stretch ratio for the stretched segment from Animal 1, etc.

Table 3. Stretch ratios for stretched and unstretched segments of septum.

| $\lambda_{animal,segment}$ | Result |
|---|---|
| $\lambda_{1U}$ | 0.98 |
| $\lambda_{2U}$ | 1.01 |
| $\lambda_{1S}$ | 1.35 |
| $\lambda_{2S}$ | 1.37 |

**MYOCYTE DEFORMATIONS**

At the cellular level, the deformation measure of interest was the ratio of the second moments of the area, $\rho$. Using an unpaired t test, we compared the distributions of $\rho_{affine}$ and $\rho_{actual}$ to determine whether the cells moved affinely when the samples were stretched; we also compared $\rho_{undeformed}$ and $\rho_{actual}$. The p-values from these tests are summarized in Table 4.

Table 4. Summary of p-values from unpaired t tests on $\rho$ distributions.

| Model | Ratios of Interest | |
|---|---|---|
| | $\rho_{affine}$ & $\rho_{actual}$ | $\rho_{undeformed}$ & $\rho_{actual}$ |
| Animal 1 | p = 4.4631e-14 | p = 0.0336 |
| Animal 2 | p = 0 | p = 0.2879 |

Figs. 15-20 are histograms and box plots comparing the $\rho$ distributions for the undeformed case with the distributions for the affine and actual cases. Visual inspection of the box plots, in particular, reveals that $\rho_{actual}$ and $\rho_{affine}$ are very different; in fact, $\rho_{undeformed}$ and $\rho_{actual}$ seem to be more similar. The Matlab code used to generate these plots is available in Appendix A.
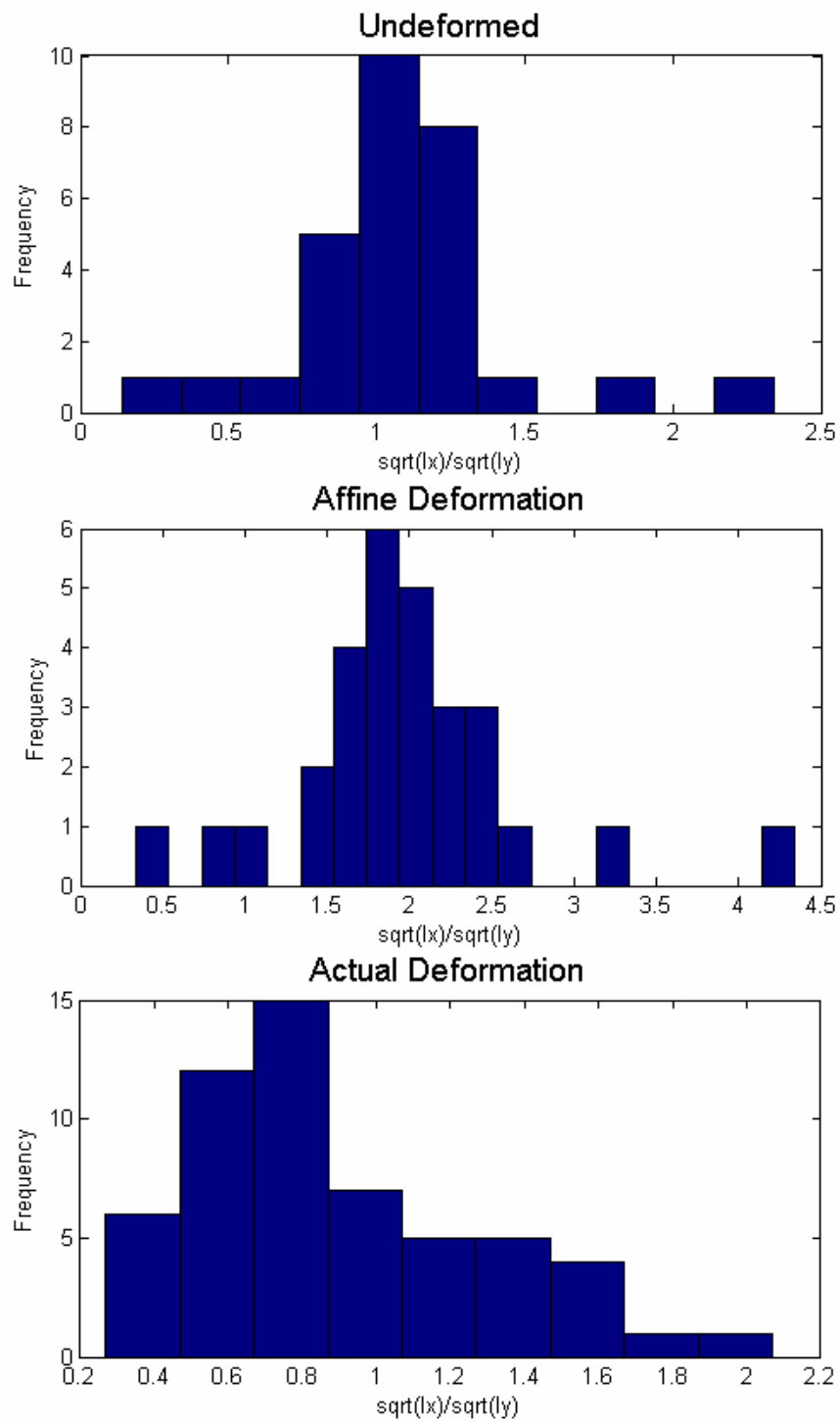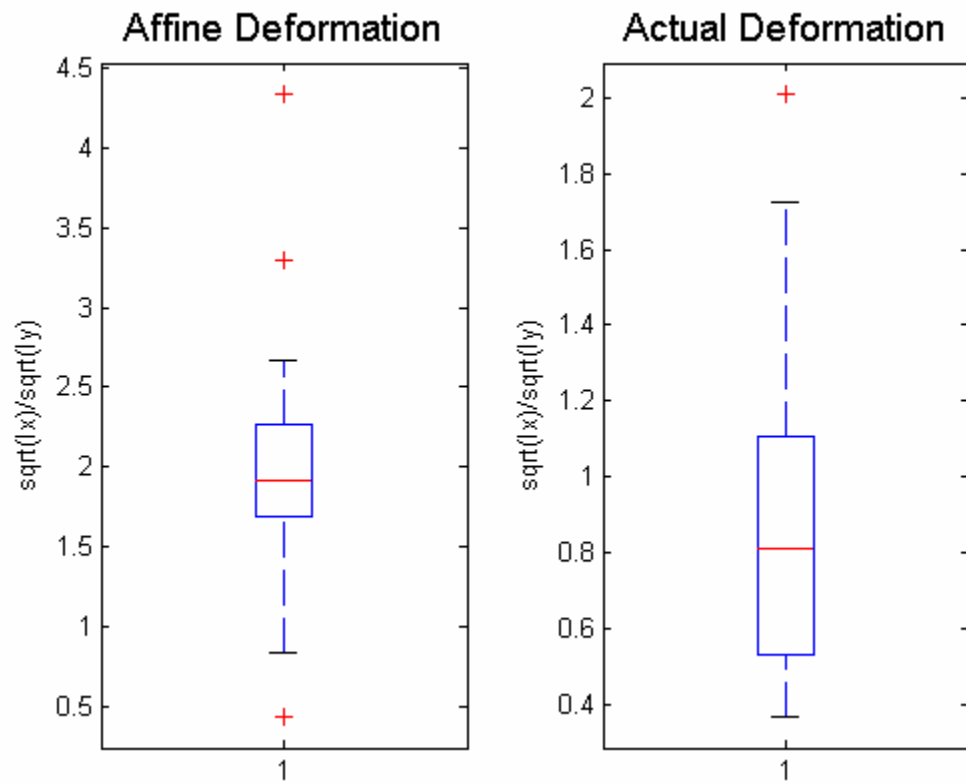
Fig. 15. Histograms of ρ distributions for Animal 1.

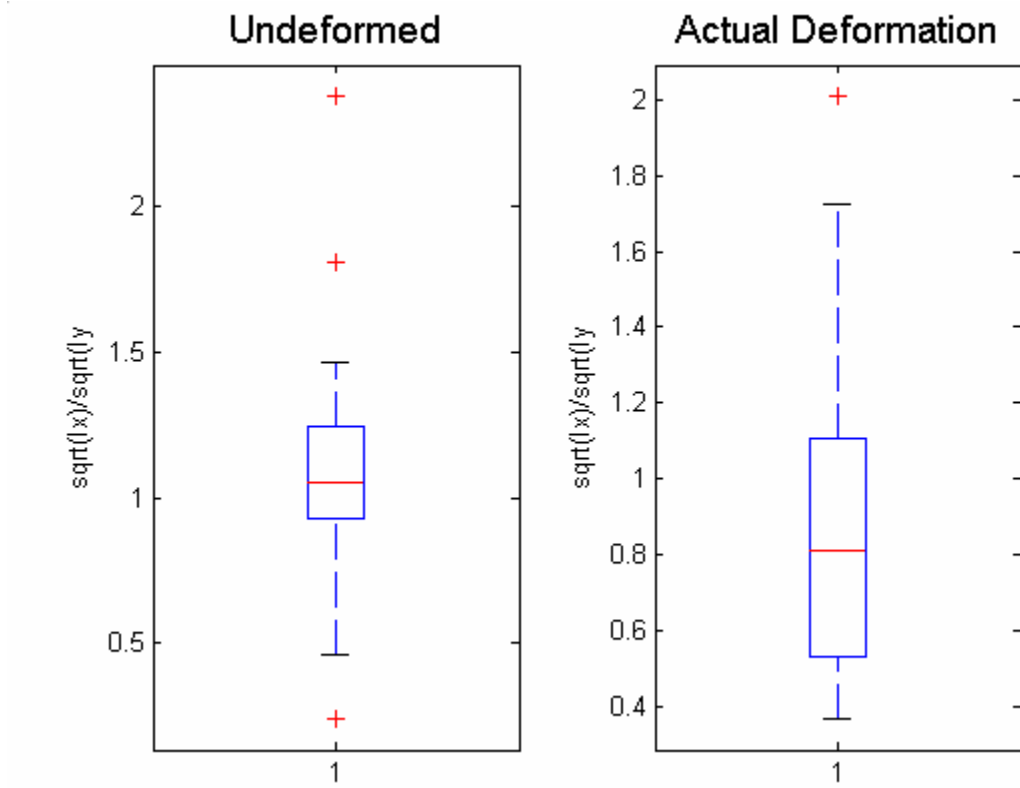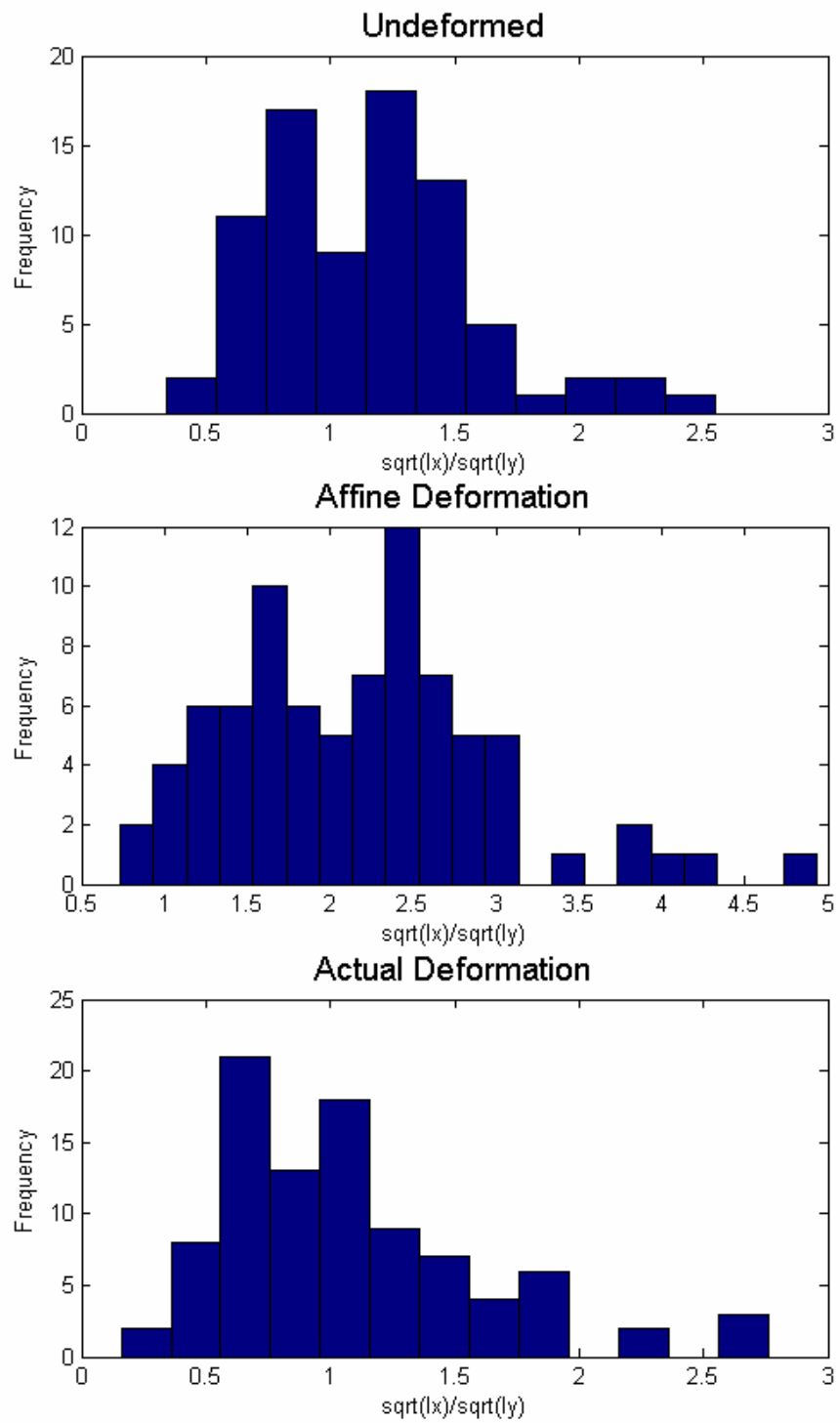Fig. 16. Box plots comparing $\rho_{affine}$ and $\rho_{actual}$ for Animal 1.

Fig. 17. Box plots comparing $\rho_{undeformed}$ and $\rho_{actual}$ for Animal 1.
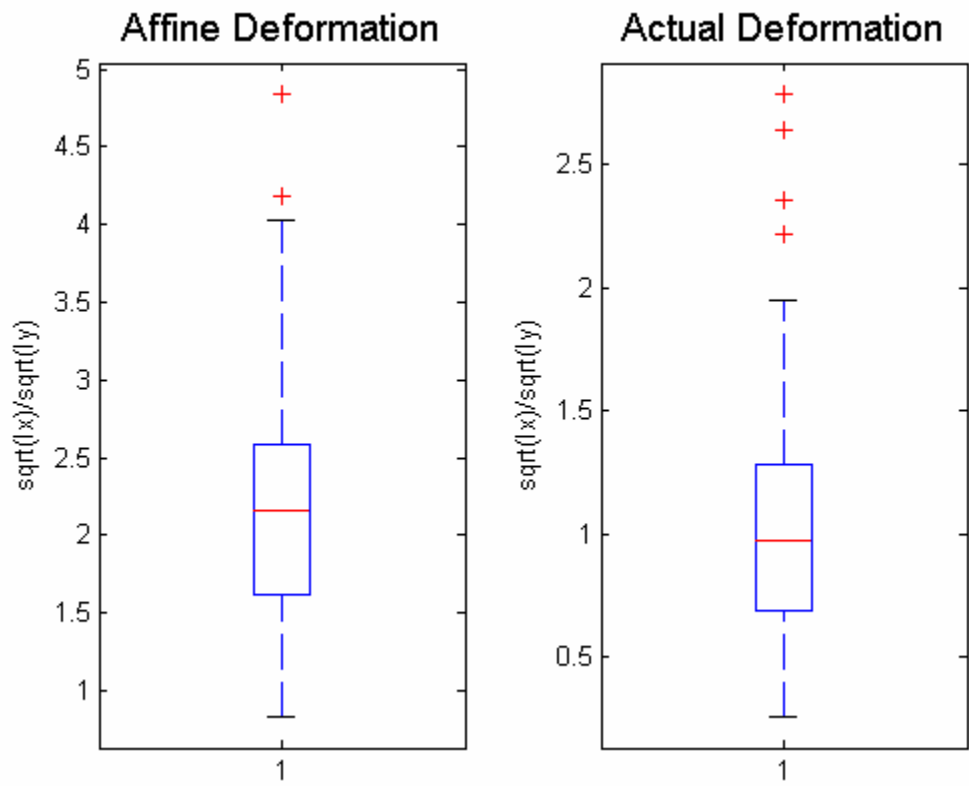
Fig. 18. Histograms of ρ distributions for Animal 2.

Fig. 19. Box plots comparing $\rho_{affine}$ and $\rho_{actual}$ for Animal 2.
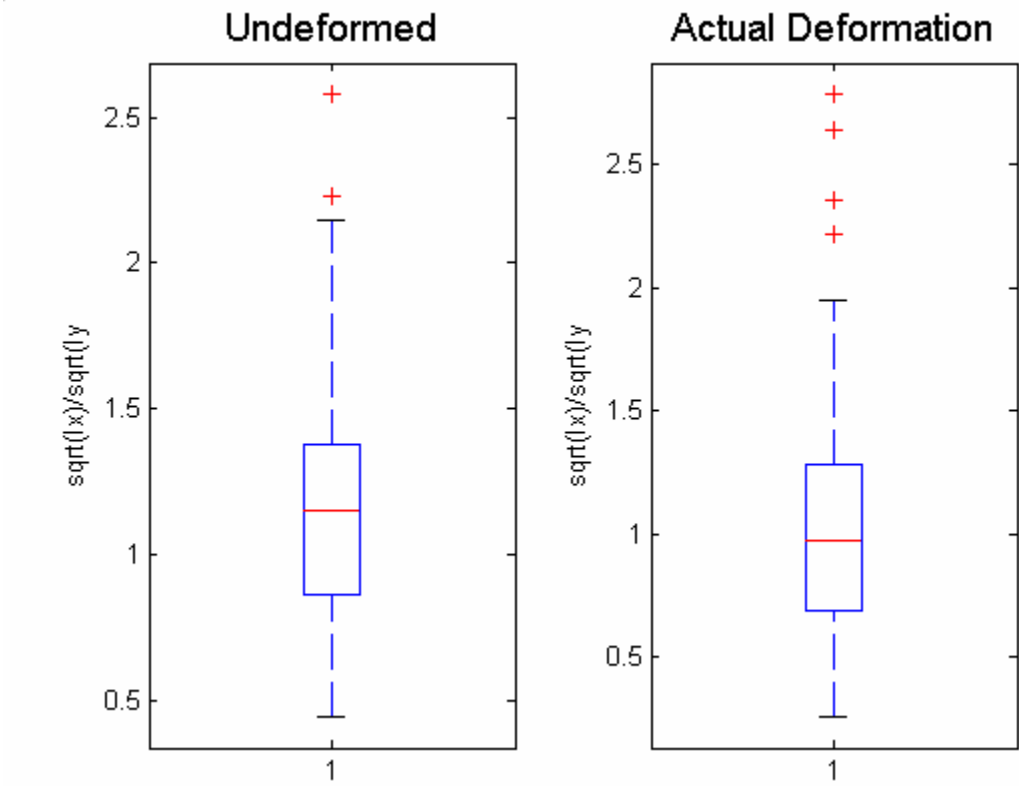
Fig. 20. Box plots comparing $\rho_{undeformed}$ and $\rho_{actual}$ for Animal 2.

# CHAPTER V

# DISCUSSION

Quantifying a relationship between macroscopic myocardial strain and myocyte deformation would allow for the formulation of better constitutive relationships. Currently, there is only a very limited understanding of the changes in myocyte geometry that accompany deformations of the ventricles. Based on theoretical models and biaxial tests, several studies suggest that non-axial deformations may significantly contribute to the underlying mechanism of ventricular contraction; they also highlight the need for more information about the nature of myocyte deformation (Lin and Yin, 1998; Zahalak, 1996, 1999). In an attempt to provide this information, we established experimental protocols and selected an imaging technique that allowed us to examine stretched myocardium at the cellular level.

Prior to performing a statistical analysis of our data, we selected a significance level of 0.05. This selection required that, when comparing $\rho$ distributions, we obtain p-values less than 0.05 in order to say that the distributions were significantly different. When we compared $\rho$ for an affine deformation with $\rho$ for the actual deformations, the resulting p-values were indeed less than 0.05 (see Table 4), indicating that the myocyte deformations were non-affine in both specimen.

To determine the degree of affinity, we compared $\rho$ for the undeformed cells with $\rho$ for the actual deformations. However, our results in this case varied based on the animal model in use. For Animal 2, we obtained a p-value greater than 0.05, which

indicates that there was no statistically significant difference between the distributions for $\rho_{undeformed}$ and $\rho_{actual}$. This result implies that the myocyte deformations were completely non-affine and that only cellular rearrangement occurred upon stretching of the specimen. The result for Animal 1, however, was different, with a p-value less than 0.05. This variability may be due to inconsistencies in cell selection or simply the small number of specimen used in our experiments; in any case, the lack of a consistent result means that we are unable to say with certainty to what degree the myocyte deformations were affine.

Although we defined specific criteria for cell selection, our method of analysis allows user error because it requires the investigator to select points on an image, and the manner in which these points are selected clearly affects the results obtained. For demonstration, we repeated our stretch ratio analysis several times, selecting different but plausible points of measurement on each repetition. Comparing the stretch ratios measured from a single image, we found variablities of up to 2.5%. While this error itself is small, the fact that many images were used in our analysis and many points were selected on these images means that this error could be multiplied several times. This kind of error is not limited to our stretch ratio measurements; in fact, due to the increased number of measurements, it is probably more prevalent in our analysis of cell size. While every effort was made to consistently choose points in accordance with our protocols, the very method by which we gathered data inevitably introduces a measure of error.

       Despite its novelty, our experimental methods had numerous limitations and would benefit from several improvements.  While any information about changes in myocyte geometry would be helpful in developing constitutive relationships, the uniaxial stretching we performed is not representative of the ventricular deformations that occur during contraction; biaxially stretched myocardium subjected to the same kind of analysis would provide more complete data.  In addition, because cardiac myocytes tend to be irregularly shaped, the same sample should be imaged stretched and unstretched, rather than using two samples (i.e., anterior and posterior segments) from one septum.  Also, because elastin cannot be fixed in formalin, release of stretched, formalin-fixed tissue from the stretching device can cause recoil and bucking of the sample; use of fresh tissue would eliminate recoil and any resulting tissue distortion.  However, the use of fresh tissue would necessitate the development of an improved stretching device that allows the sample to be imaged while still attached to the device.  It would also be interesting to label individual cells with fluorescent markers and follow their deformation and/or rearrangement as the sample is stretched.

**CHAPTER VI**

**CONCLUSION**

Affecting over 18,000,000 people, heart disease is the leading cause of death for adults in this country (American Heart Association, 2003). In the year 2004 alone, an estimated 1.2 million Americans will suffer at least one heart attack; 500,000 of these will be recurrent attacks. As our population ages and the incidence of cardiovascular disease continues to rise, there will be a need for more effective therapies and treatments. However, the development of such treatments is contingent upon an increased understanding of the mechanical properties of myocardium and the underlying nature of ventricular contraction.

Data on the cellular deformations resulting from ventricular contraction is very limited. Such data is necessary in order to formulate better constitutive relations for myocardium, which would lead to more accurate whole-heart models and, ultimately, to better therapies for diseased hearts. Due to the lack of information about the relationship between macroscopic and cellular deformations, the goal of this project was to develop an experimental method to examine these deformations and to determine their degree of affinity. A set of protocols was established for specimen preparation, image acquisition, and analysis, and two experiments were performed according to these methods.

While current models of myocardium assume that myocytes deform affinely when myocardium is deformed, our results show that cellular deformations are non-affine. Variability in our data leads to uncertainty about the degree of affinity, but it

appears that myocyte deformations may be completely non-affine; in this case, cells would not stretch at all but would simply rearrange to produce the observed macroscopic deformations. Because our results were inconsistent, more investigation is needed in this area.

Although we have determined that myocytes do not deform affinely when myocardium is stretched, a need remains to quantify the relationship between ventricular deformation and changes in myocyte geometry. While our results do not allow us to mathematically define this relationship, we are able to suggest improved experimental methods that should lead future investigators to this information. When combined with our current knowledge of the mechanism of ventricular contraction, this information could result in significantly improved models of myocardium and, subsequently, a better understanding of how to heal the diseased heart.

**REFERENCES**

American Heart Association, 2003. Heart Disease and Stroke Statistics – 2004 Update. American Heart Association, Dallas.

Bagni, M.A., Cecchi, G. and Colomo, F., 1990.  Myofilament spacing and force generation in intact frog muscle fibers, Journal of Physiology 430, 61-75.

Carew, T.E. and Covell, J.W., 1979. Fiber orientation in hypertrophied canine left ventricle. American Journal of Physiology 263, H487-H493.

Costa, K.D., May-Newman, K., Farr, D., O'Dell, W.G., McCulloch, A.D. and Omens, J.H., 1997. Three-dimensional residual strain in midanterior canine left ventricle. American Journal of Physiology 273, H1968-H1976.

Costa, K.D., Takayama, Y., McCulloch, A. and Covell, J.W., 1999. Laminar fiber architecture and three-dimensional systolic mechanics in canine ventricular myocardium. American Journal of Physiology 276, H595-H607.

Costa, K.D., Holmes, J.W. and McCulloch, A.D., 2001a. Modelling cardiac mechanical properties in three dimensions. Philosophical Transactions of the Royal Society of London 359, 1233-1250.

Costa, K.D., May-Newman, K., Farr, D., O'Dell, W.G., McCulloch, A.D. and Omens, J.H., 2001b. Three-dimensional residual strain in midanterior canine left ventricle. American Journal of Physiology 273, H1968-H1976.

Emery, J.L. and Omens, J.H.,1997. Mechanical regulation of myocardial growth during volume-overload hypertrophy in the rat. American Journal of Physisology 273, H1198-H1204.

Florenzano, F., and Glantz, S.A., 1987. Left ventricular mechanical adaptation to chronic aortic regurgitation in intact dogs. American Journal of Phsyiology. 252, H969-H984.

Fung, Y.C., 1993. Biomechanics: Mechanical Properties of Living Tissue (2$^{nd}$ Edn). Springer-Verlag, New York.

Gerdes, A.M. and Capasso, 1995. J.M. Structural remodeling and mechanical dysfunction of cardiac myocytes in heart failure. Journal of Molecular and Cellular Cardiology 27, 849-856.

Goldman, Y.E., 1987. Measurement of sarcomere shortening in skinned fibers from frog muscle by white light diffraction. Biophysical Journal 52, 57-68.

Goldman, Y.E. and Simmons, R.M., 1986. The stiffness of frog skinned muscle fibers at altered lateral filament spacing. Journal of Physiology 311, 219-249.

Grossman, W., 1980. Cardiac hypertrophy: useful adaptation or pathologic process? American Journal of Medicine 69, 576-583.

Humphrey, J.D., Strumpf, R.K. and Yin, Y.C.P., 1990. Determination of a constitutive relation for passive myocardium. I. A new functional form. Journal of Biomechanical Engineering 112, 333-339.

Humphrey, Jay D., 2002. Cardiovascular Solid Mechanics: Cells, Tissues, and Organs. Springer-Verlag, New York.

Huxley, H.E. and Hanson, J., 1954. Changes in the cross-striations of muscle during contraction and stretch and their structural interpretation. Nature 173, 973-976.

Huxley, H.E., 1969. The mechanism of muscular contraction. Science 164, 1356-1366.

Karlon, W.J., McCulloch, A.D., Covell, J.W., Hunter, J.J. and Omens, J.H., 2000. Regional dysfunction correlates with myofiber disarray in transgenic mice with ventricular expression of ras. American Journal of Physiology 278, H898-H906.

Krasner, B. and Maugham, D., 1984. The relationship between ATP hydrolysis and active force in compressed and swollen skinned muscle fibers of rabbit. Pflugers Archiv 400, 160-165.

LeGrice, I.J., Smaill, B.H., Chai, L.Z., Edgar, S.G., Gavin, J.B. and Hunter, P.J., 1995. Laminar structure of the heart: ventricular myocyte arrangement and connective tissue architecture in the dog. American Journal of Physiology, 38, H571-H582.

Lin, D.H. and Yin, F.C.P., 1998. A multiaxial constitutive law for mammalian left ventricular myocardium in steady-state barium contracture or tetanus. Journal of Biomechanical Engineering 120, 504-517.

MacKenna, D.A., Omens, J.H., McCulloch, A.D. and Covell, J.W., 1994. Contribution of collagen matrix to passive left ventricular mechanics in isolated rat hearts. American Journal of Physiology 266, H1997-H1018.

MacKenna, D.A., Vaplon, S.M. and McCulloch, A.D., 1997. Microstructural model of perimysial collagen fibers for resting myocardial mechanics during ventricular filling. American Journal of Physiology 273, H1576-H1586.

McLean, M., Ross, M.A. and Prothero, J., 1989. Three-dimensional reconstruction of the myofiber pattern in the fetal and neonatal mouse heart. Anatomical Record 224, 392-406.

Metzger, J.M. and Moss, R.L., 1987. Shortening velocity in skinned single muscle fibers. Biophysical Journal 52, 127-131.

Omens, J.H., 1998. Stress and strain as regulators of myocardial growth. Progress in Biophysics and Molecular Biology 69, 559-572.

Omens, J.H., Rodriguez, E.K. and McCulloch, A.D., 1996. Transmural changes in stress-free myocyte morphology during pressure overload hypertrophy in the rat. Journal of Molecular and Cellular Cardiology 28, 1975-1983.

Opie, Lionel H., 1998. The Heart: Physiology, from Cell to Circulation (3$^{rd}$ Edn). Lippincott-Raven, Philadelphia, pp. 43-63.

Opie, Lionel H., 2004. Heart Physiology from Cell to Circulation (4$^{th}$ Edn). Lippincott Williams & Wilkins, Philadelphia, pp. 42-68.

Peachey, L.D., 1978. Three-dimensional structure of muscle fiber. In Biophysical Aspects of Cardiac Muscle: Proceedings of the Cardiac Muscle Symposium. Academic Press, New York.

Robinson, Thomas F., Factor, Stephen M., and Sonnenblick, Edmund H., 1986. The heart as a suction pump. Scientific American 254, 84-91.

Smaill, B. and Hunter, P., 1991. Structure and function of the diastolic heart: material properties of passive myocardium. In Glass, L., Hunter, P.J. and McCulloch, A.D. (Eds.), Theory of Heart. Springer-Verlag, New York, pp. 1-29.

Taconic Technical Library, 2002. Hematological clinical chemistry values. Sprague-dawley rat (www.taconic.com). Accessed: August 2004.

Takayama, Y., Costa, K. and Covell, J.W., 2002. Contribution of laminar myofiber architecture to load-dependent changes in mechanics of LV myocardium. American Journal of Physiology 282, H1510-H1520.

Weber, K.T., Sun, Y.S., Tyagi, S.C. and Cleutjens, J.P.M., 1994. Collagen network of the myocardium: function, structural remodeling, and regulatory mechanisms. Journal of Molecular and Cellular Cardiology 26, 279-292.

Zahalak, G.I., 1996. Non-axial Muscle Stress and Stiffness. Journal of Theoretical Biology 182, 59-84.

Zahalak, G.I., de Laborderie, V. and Guccione, J.M., 1999. The Effects of Cross-Fiber Deformation on Axial Fiber Stress in Myocardium. Journal of Biomechanical Engineering 121, 376-385.

**APPENDIX A**

**ANNOTATED MATLAB CODES**

# Cell Selection Program

```
clear all
close all

%Allows user to input image filename.
filename = input('Input image filename now.')
I = imread(filename);
imagesc(I); hold on
load data
%output = [0 0 0 0 0 0 0 0];
s = size(output);
r = s(1)
for q=1:r
   plot(output(q,5),output(q,6),'+','color','r');
end

%Allows user to pick points on boundary of cell.
'Pick points now and press enter.'
in_pt=[4; 0];
pts_in=[];
while isempty(in_pt) == 0
   in_pt = round(ginput(1))';
   if isempty(in_pt) == 0
      plot(in_pt(1),in_pt(2),'r.');
      pts_in=[pts_in in_pt]
   end
end

%pts_in will be the array of pixel coordinates.
 pts_in = [pts_in]';
n = size(pts_in,1);
pts_centroid = sum(pts_in)/n;
pts_in=[pts_in; pts_in(1,:)];

%Plots the given pixels.
figure(1)
plot (pts_in(1,:), pts_in(2,:),'o'); hold on

%Plots the centroid.
plot(pts_centroid(:,1),pts_centroid(:,2),'+')
pts_boundry = [];
```

*% D will be an array of the lengths of the sides.*
D=[];

*% i will iterate the x values, while j iterates the y values.*
for i = 1:n;
   d = sqrt((pts_in(i,1) - pts_in(i+1,1))^2 + (pts_in(i,2) - pts_in(i+1,2))^2);
   D = cat(1,D,d);
end

*% sides will be an array of all the pixels along the outer edge.*
sides = [];
for k=1:n;
   n_seg_pts = round(1.25*(D(k)));
   for q=1:n_seg_pts;
      x = round(pts_in(k,1)+(pts_in(k+1,1)-pts_in(k,1))*(q/n_seg_pts));
      y = round(pts_in(k,2)+(pts_in(k+1,2)-pts_in(k,2))*(q/n_seg_pts));
      sides = [sides;x y];
   end
   k = k+1;
end
figure(2)
plot(sides(:,1),sides(:,2),'o')
n_s_pts = size(sides,1);
sides = sortrows(sides,2);
y_min = sides(1,2);
y_max = sides(n_s_pts,2);
n_ys = y_max - y_min +1;
lft_x = zeros(n_ys,1);
rt_x = zeros(n_ys,1);
i=1;
j=1;
while j < n_ys
   begin_i = i;
   while sides(i,2) == sides(i+1,2)
      i = i+1;
      end_i = i;
   end
   lft_x(j+1) = min(sides(begin_i:end_i,1));
   rt_x(j+1) = max(sides(begin_i:end_i,1));
   j = j+1;
   i = i+1;
end

   solid_pts = [];

```matlab
for i = 1:n_ys
        for j = lft_x(i):rt_x(i)
                solid_pts = [solid_pts; j i-1+y_min];
    end
end
m = size(solid_pts,1);
centroid = sum(solid_pts)/m;
r_vecs=sides-ones(n_s_pts,1)*centroid;
r_tensor_r=[sum(r_vecs(:,1).*r_vecs(:,1)) sum(r_vecs(:,1).*r_vecs(:,2));
        sum(r_vecs(:,2).*r_vecs(:,1)) sum(r_vecs(:,2).*r_vecs(:,2))]/m;
[tmp_dirs tmp_vals]=eig(r_tensor_r);
if tmp_vals(1,1) >= tmp_vals(2,2)
    major_val=tmp_vals(1,1); minor_val=tmp_vals(2,2);
    major_vec=tmp_dirs(:,1); minor_vec=tmp_dirs(:,2);
else
    major_val=tmp_vals(2,2); minor_val=tmp_vals(1,1);
    major_vec=tmp_dirs(:,2); minor_vec=tmp_dirs(:,1);
end

maj_to_min_ratio = sqrt(major_val/minor_val)
%   minor_lngth=sqrt(minor_val)*2;
minor_lngth=sqrt(m/(pi*maj_to_min_ratio))*2
major_lngth=maj_to_min_ratio*minor_lngth
area=m
figure(3)
plot(solid_pts(:,1),solid_pts(:,2),'.'); hold on


major_axis_vector=major_vec
alpha=atan2(minor_vec(2),minor_vec(1));
if alpha < 0; alpha=alpha+2*pi; end
tmp_pts=[centroid+major_lngth*major_vec'/2; centroid-major_lngth*major_vec'/2];
plot(tmp_pts(:,1),tmp_pts(:,2),'c')
plot(tmp_pts(:,1),tmp_pts(:,2),'k+')
tmp_pts=[centroid+minor_lngth*minor_vec'/2; centroid-minor_lngth*minor_vec'/2];
plot(tmp_pts(:,1),tmp_pts(:,2),'r')
plot(tmp_pts(:,1),tmp_pts(:,2),'k+')
axis('image')
plot(centroid(:,1),centroid(:,2),'+','color','r'); axis('image')
cent_x = centroid(:,1);
cent_y = centroid(:,2);
```

num_pixels_in_cell=m

*%Calculates second moments of the area.*
m2y = sqrt(sum((solid_pts(:,2)-ones(m,1)*centroid(2)).^2)/m)
m2x = sqrt(sum((solid_pts(:,1)-ones(m,1)*centroid(1)).^2)/m)
mxy = sum((solid_pts(:,1)-ones(m,1)*centroid(1)).*(solid_pts(:,2)-
ones(m,1)*centroid(2)))/m
%m2xnew= sqrt(m2x^2*(cos(alpha))^2 + m2y^2*(sin(alpha))^2 -
2*mxy*(cos(alpha))*(sin(alpha)));
%m2ynew= sqrt(m2y^2*(cos(alpha))^2 + m2x^2*(sin(alpha))^2 +
2*mxy*(cos(alpha))*(sin(alpha)));
x_to_y_ratio = m2x/m2y;

output = [output; x_to_y_ratio m2x m2y num_pixels_in_cell cent_x cent_y mxy
alpha];

*%Writes output data to file.*
save data output
%wk1write('E:\data',output);

**Stretch Ratio Program**

```
clear all
close all

%Prompts user to input filename and loads image file.
filename1 = input('Input unstretched image filename now.')
I = imread(filename1);
imagesc(I); hold on

%Prompts user to input unstretched coordinates and calculates unstretched length.
'Choose Ymax (unstretched) now.'
YmaxU = round(ginput(1));
plot(YmaxU(1),YmaxU(2),'r.');
'Choose Ymin (unstretched) now.'
YminU = round(ginput(1));
plot(YminU(1),YminU(2),'r.');
'Choose high number on ruler.'
A = round(ginput(1));
plot(A(1),A(2),'r.');
HighP = A(2);
HighPM = input('Enter measurement (cm) from high number and press enter.');
'Choose low number on ruler.'
B = round(ginput(1));
plot(B(1),B(2),'r.');
LowP = B(2);
LowPM = input('Enter measurement (cm) from low point and press enter.');
Ratio1 = ((HighPM-LowPM)./(HighP-LowP));
LengthU = Ratio1*(YmaxU-YminU);
hold off

%Repeats processed with stretched image.
filename2 = input('Input stretched image filename now.')
I = imread(filename2);
imagesc(I); hold on

%Prompts user to input stretched coordinates and calculates unstretched length.
'Choose Ymax (stretched) now.'
YmaxS = round(ginput(1));
plot(YmaxS(1),YmaxS(2),'r.');
'Choose Ymin (stretched) now.'
YminS = round(ginput(1));
plot(YminS(1),YminS(2),'r.');
'Choose high number on ruler.'
```

```
C = round(ginput(1));
plot(C(1),C(2),'r.');
HighQ = C(2);
HighQM = input('Enter measurement (cm) from high number and press enter.');
'Choose low number on ruler.'
D = round(ginput(1));
plot(D(1),D(2),'r.');
LowQ = D(2);
LowQM = input('Enter measurement (cm) from low number and press enter.');
Ratio2 = ((HighQM-LowQM)/(HighQ-LowQ));
LengthS = Ratio2*(YmaxS-YminS);

%Calculates stretch ratio.
StretchRatio = LengthS/LengthU
```

## P-Value Calculation and Histogram Plotting Program

```
clear all
close all
```

*%Prompts user to input sheet name and plots histograms for unstretched data.*
```
Filename1 = input('Input file name for unstretched specimen.')
Sheetname1 = input('Input sheet name for unstretched specimen.')
A=xlsread(Filename1,Sheetname1);
MA=mean(A);
SA=std(A);
x=min(A):.2:max(A);
subplot(3,1,1); hist(A,x);
xlabel('sqrt(Ix)/sqrt(Iy)'); ylabel('Frequency');
title('Undeformed','FontSize',14);
Ratio = input('Input stretch ratio.')
NA = numel(A);
```

*%Calculates Ix/Iy for an affine deformation with a given stretch ratio.*
```
B=A.*(Ratio^2);
MB=mean(B);
SB=std(B);
y=min(B):.2:max(B);
subplot(3,1,2); hist(B,y);
xlabel('sqrt(Ix)/sqrt(Iy)'); ylabel('Frequency');
title('Affine Deformation','FontSize',14);
```

*%Prompts user to input sheet name and plots histograms for stretched data.*
```
Filename2 = input('Input file name for stretched specimen.')
Sheetname2 = input('Input sheet name for stretched specimen.')
C=xlsread(Filename2,Sheetname2);
MC=mean(C);
SC=std(C);
NC=numel(C);
z=min(C):.2:max(C);
subplot(3,1,3); hist(C,z);
xlabel('sqrt(Ix)/sqrt(Iy)'); ylabel('Frequency');
title('Actual Deformation','FontSize',14);
```

*%Generates box plots of deformations.*
```
figure(2)
subplot(1,2,1); boxplot(B);
xlabel(' '); ylabel('sqrt(Ix)/sqrt(Iy)');
title('Affine Deformation','FontSize',14);
```

```
subplot(1,2,2); boxplot(C);
xlabel(' '); ylabel('sqrt(Ix)/sqrt(Iy)');
title('Actual Deformation','FontSize',14);

figure(3)
subplot(1,2,1); boxplot(A);
xlabel(' '); ylabel('sqrt(Ix)/sqrt(Iy');
title('Undeformed','FontSize',14);
subplot(1,2,2); boxplot(C);
xlabel(' '); ylabel('sqrt(Ix)/sqrt(Iy');
title('Actual Deformation','FontSize',14);

%Calculates the p-value.
NTotal=NA+NC
PooledSD=sqrt((((NA-1)*SB^2) + ((NC-1)*SC^2))/(NA+NC-2));
SEdiff=PooledSD*(sqrt(1/NA + 1/NC));
t=(MB-MC)/SEdiff;
p=2*(1-tcdf(abs(t),NTotal-2))

%PooledSD=sqrt((((NA-1)*SA^2) + ((NC-1)*SC^2))/(NA+NC-2));
%SEdiff=PooledSD*(sqrt(1/NA + 1/NC));
%t=(MA-MC)/SEdiff;
%p=2*(1-tcdf(abs(t),NTotal-2))
```

**APPENDIX B**

**MICROGRAPHS WITH CELL MARKERS**
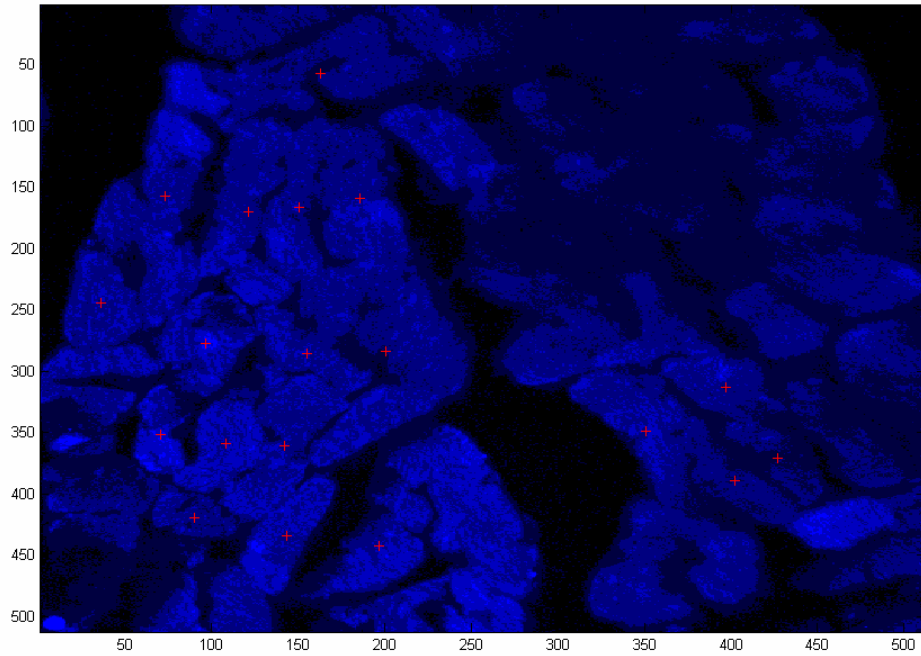
Fig. 21. Micrograph from anterior segment of Animal 1, image A1-1 (60x).
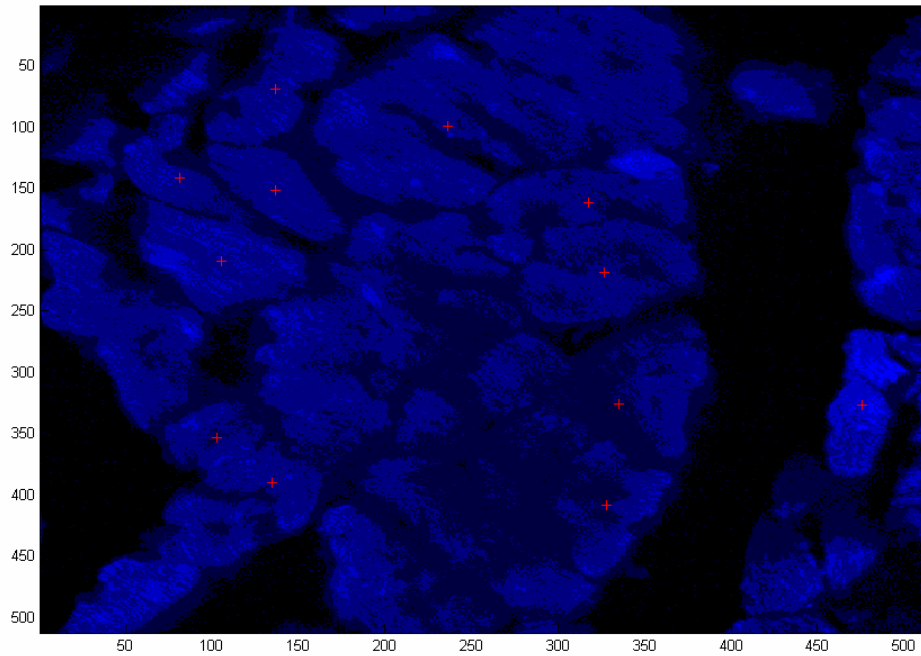


Fig. 22. Micrograph from anterior segment of Animal 1, image A1-2 (60x).
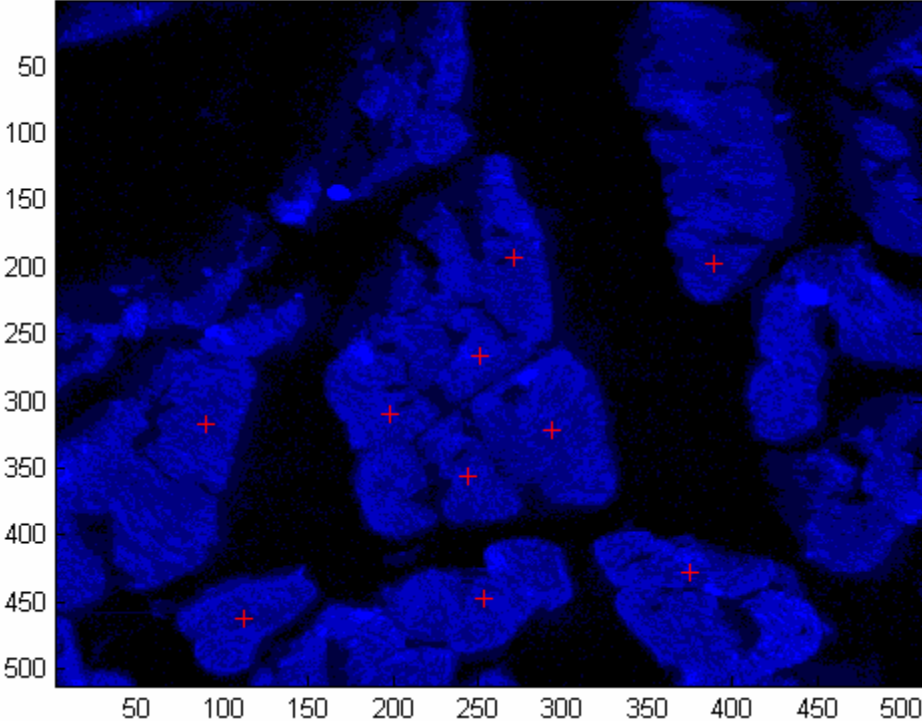
Fig. 23. Micrograph from anterior segment of Animal 1, image A1-3 (60x).
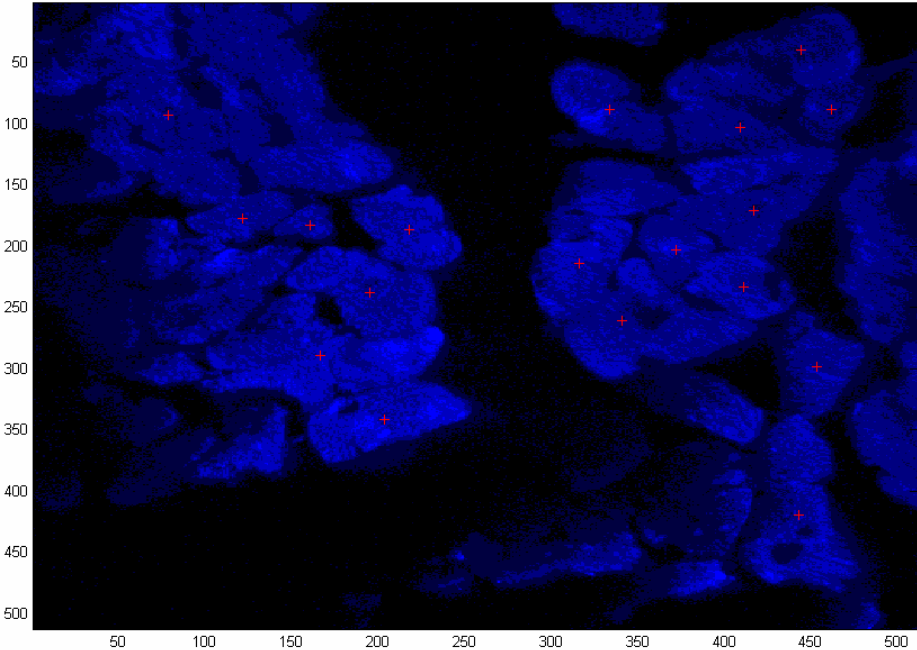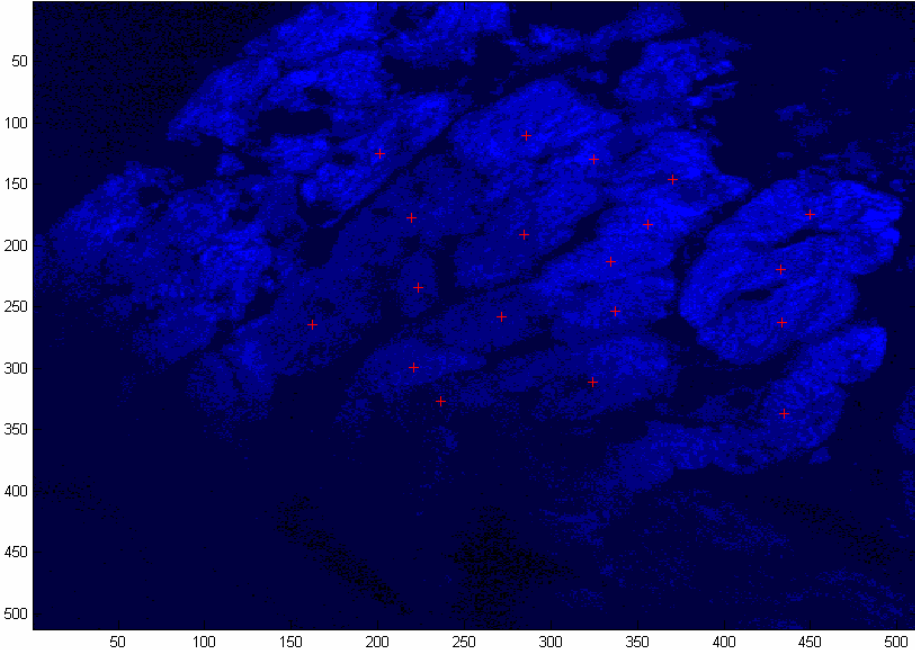


Fig. 24. Micrograph from anterior segment of Animal 1, image A1-4 (60x).
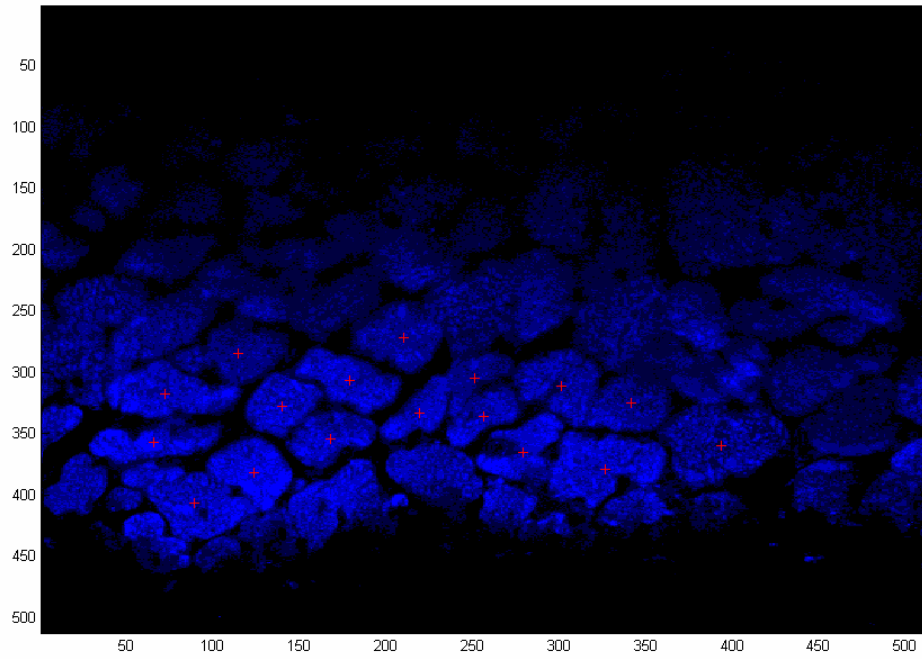
Fig. 25. Micrograph from posterior segment of Animal 1, image P1-1 (60x).
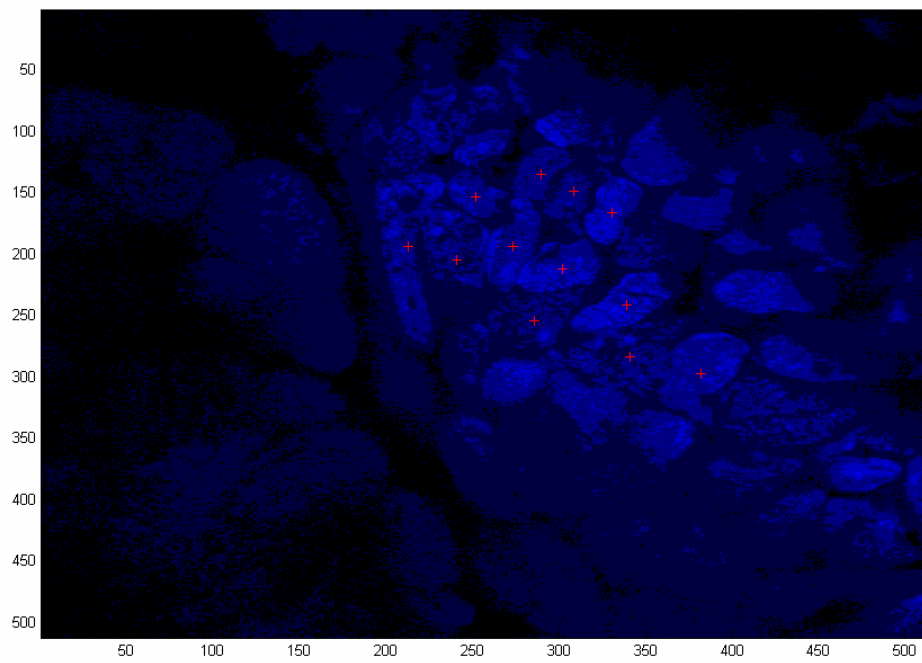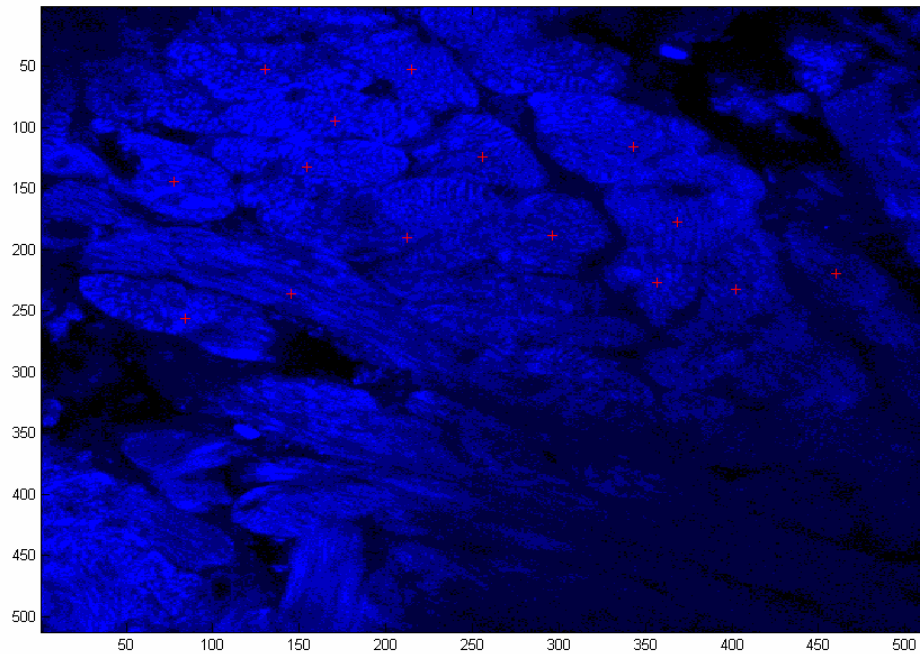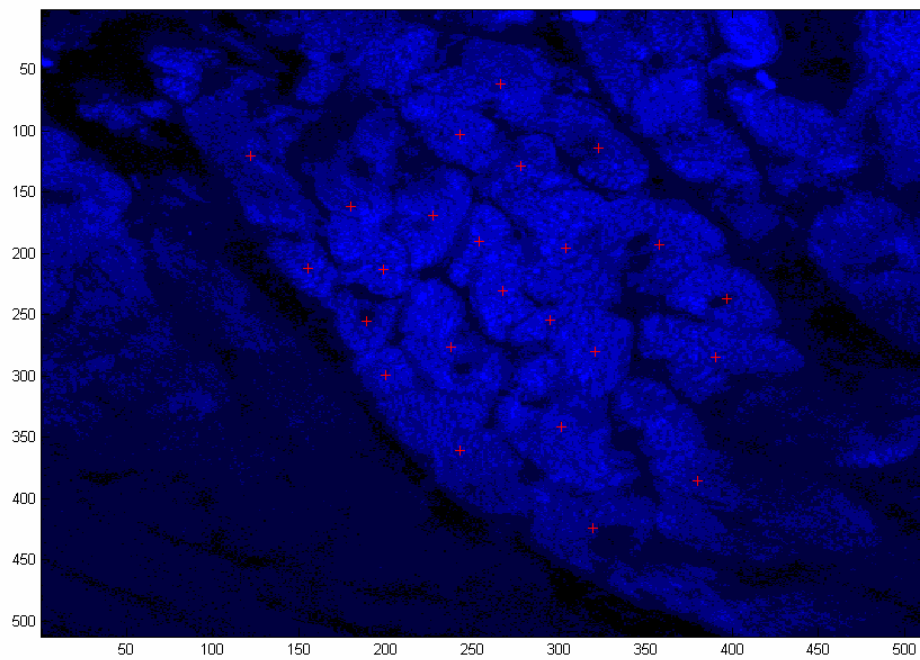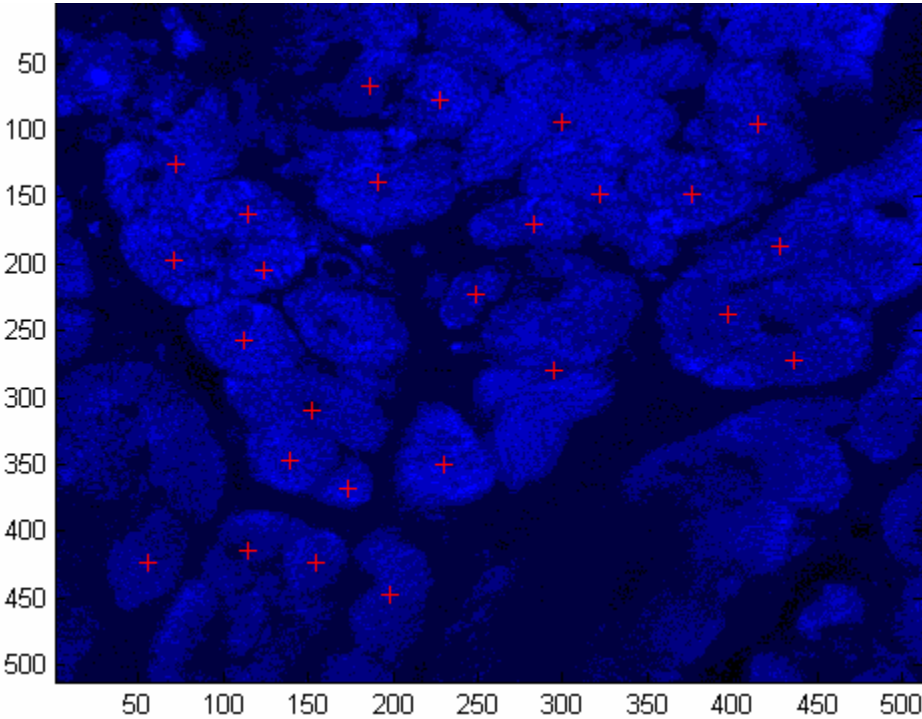


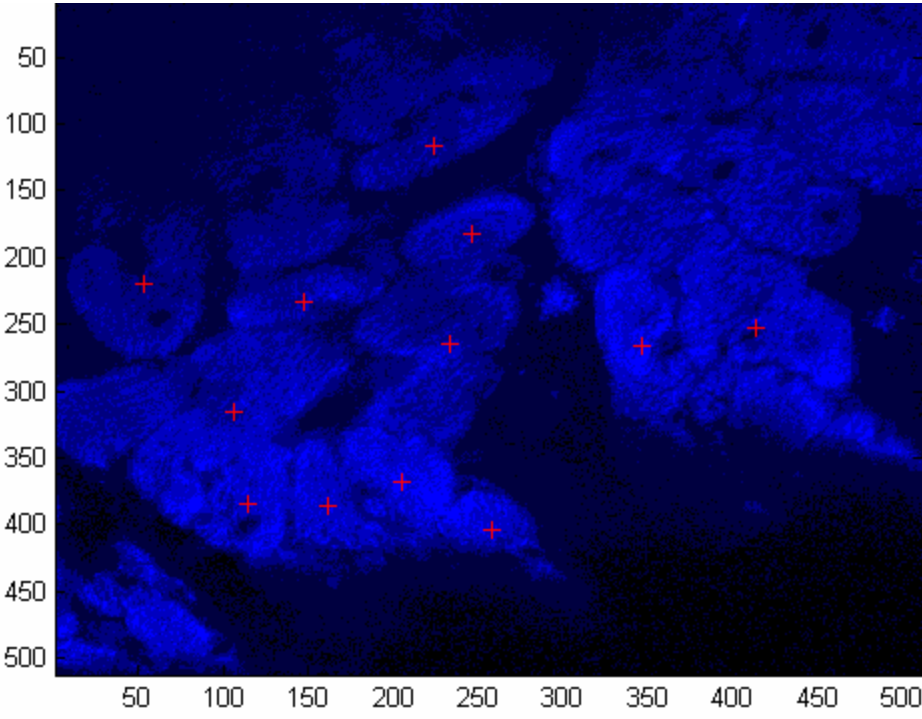Fig. 26. Micrograph from posterior segment of Animal 1, image P1-2 (60x).
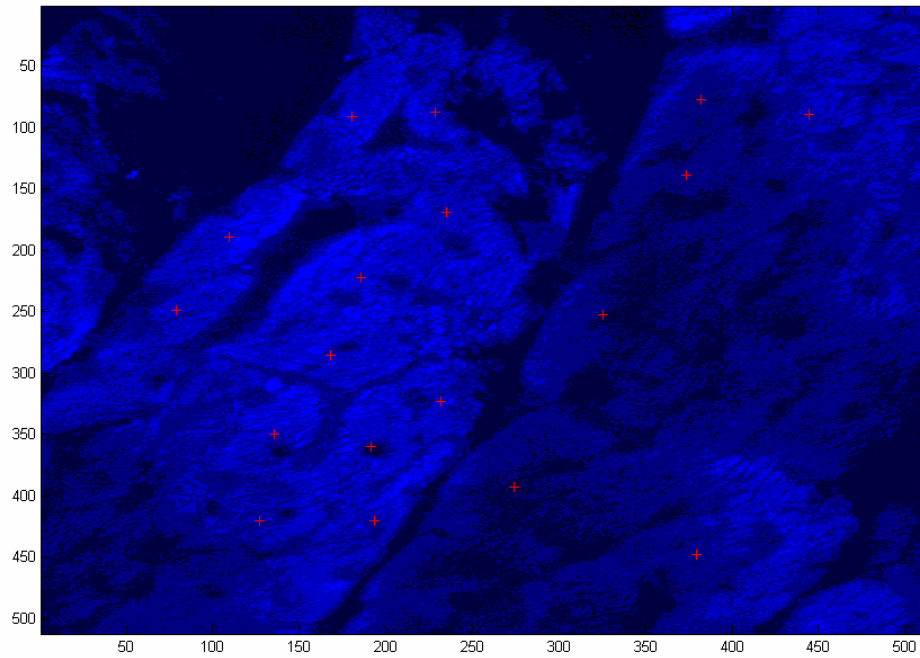
Fig. 27. Micrograph from anterior segment of Animal 2, image A2-1 (60x).
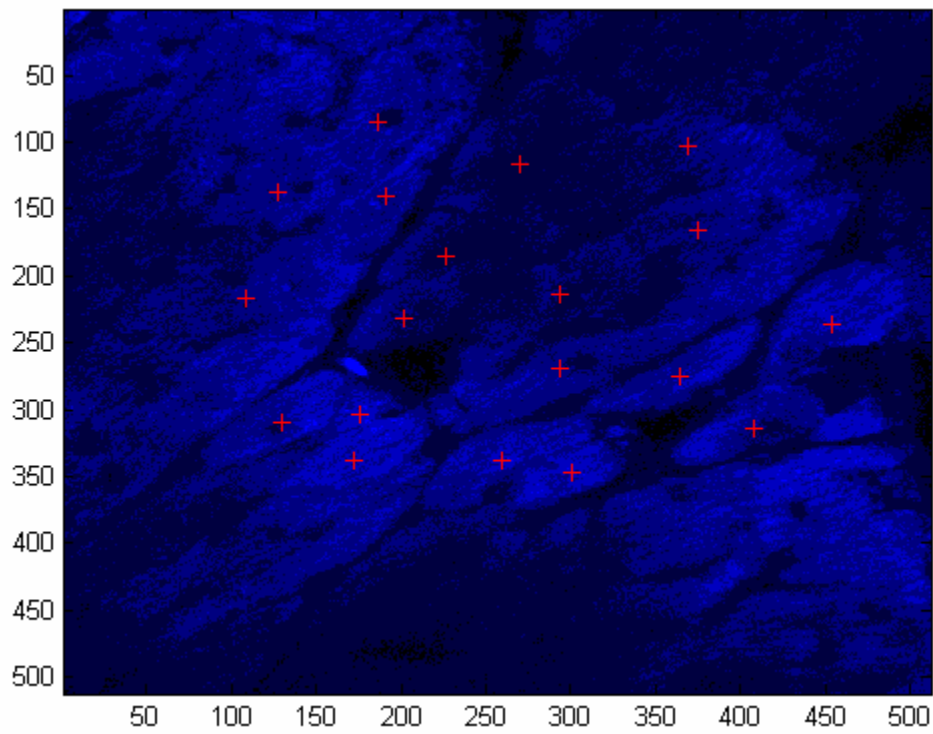


Fig. 28. Micrograph from anterior segment of Animal 2, image A2-2 (60x).
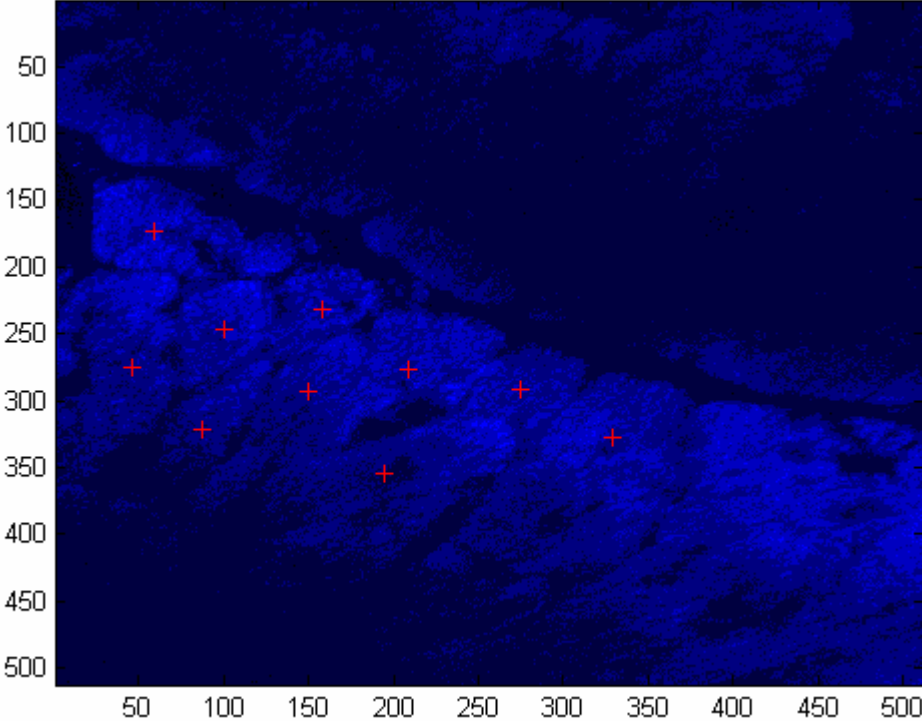
Fig. 29. Micrograph from anterior segment of Animal 2, image A2-3 (60x).
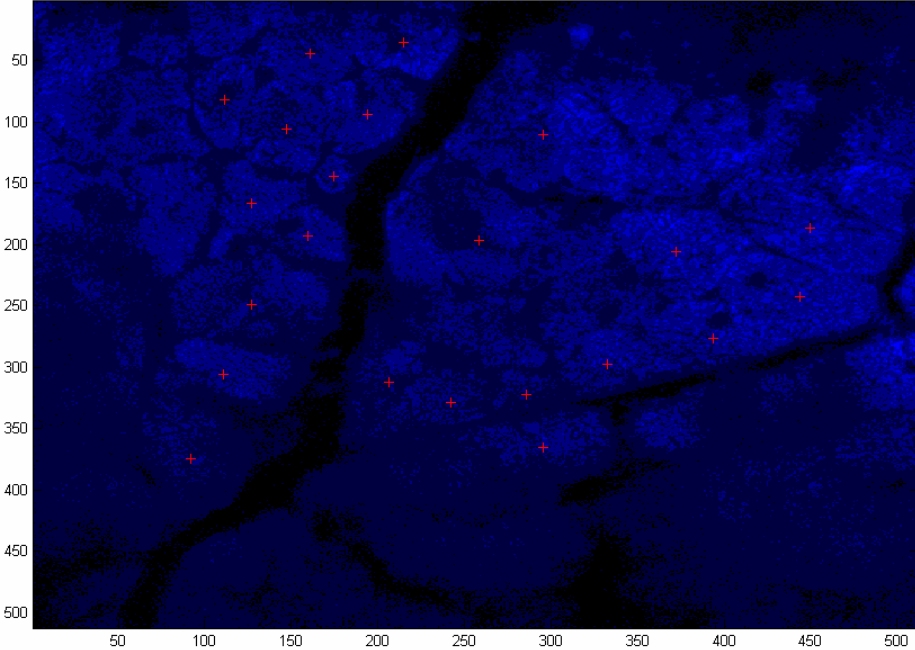


Fig. 30. Micrograph from anterior segment of Animal 2, image A2-4 (60x).
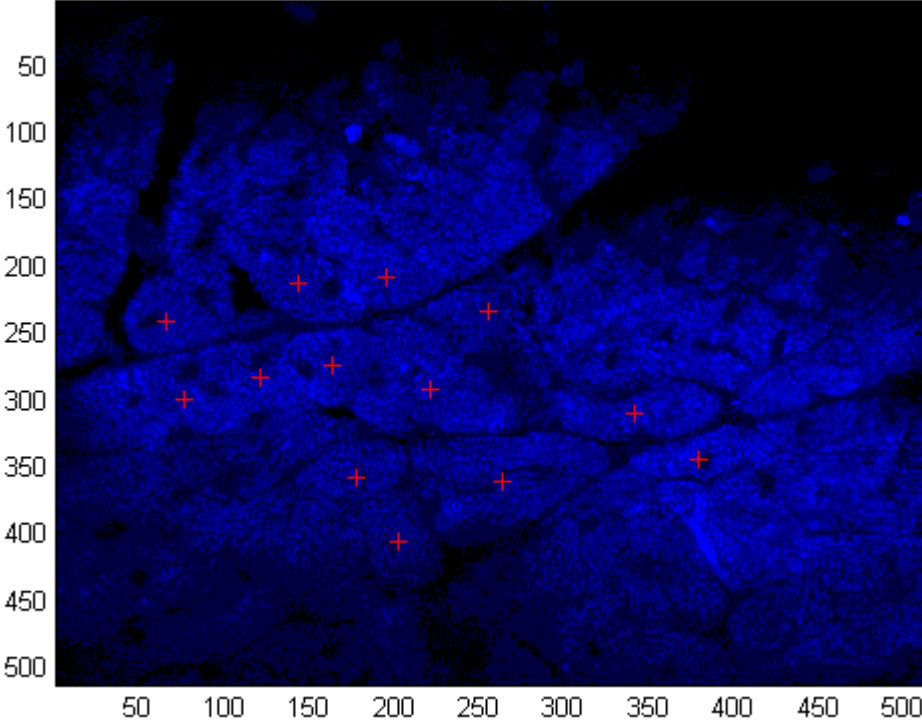
Fig. 31. Micrograph from anterior segment of Animal 2, image A2-5 (60x).



Fig. 32. Micrograph from posterior segment of Animal 2, image P2-1 (60x).

Fig. 33. Micrograph from posterior segment of Animal 2, image P2-2 (60x).



Fig. 34. Micrograph from posterior segment of Animal 2, image P2-3 (60x).

Fig. 35. Micrograph from posterior segment of Animal 2, image P2-4 (60x).



Fig. 36. Micrograph from posterior segment of Animal 2, image P2-5 (60x).

**APPENDIX C**

**PHOTOS USED FOR STRETCH RATIO CALCULATION**
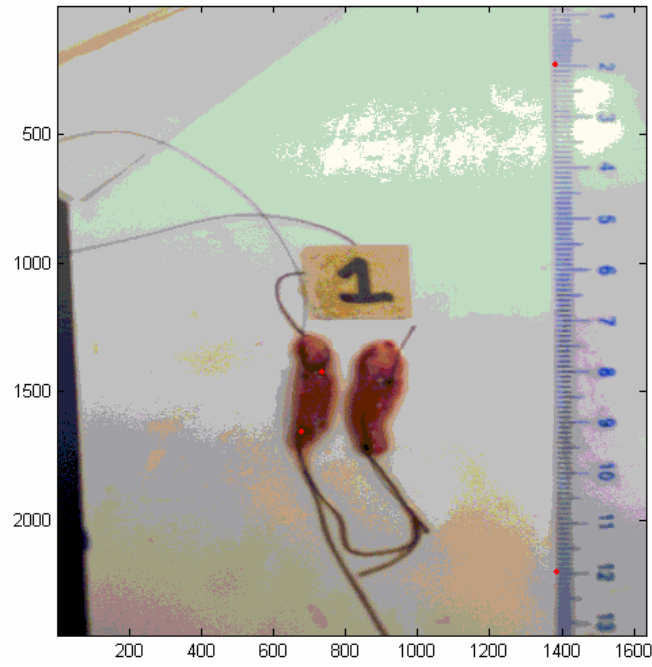
Fig. 37. Unstretched septum with marker points on anterior segment (Animal 1).
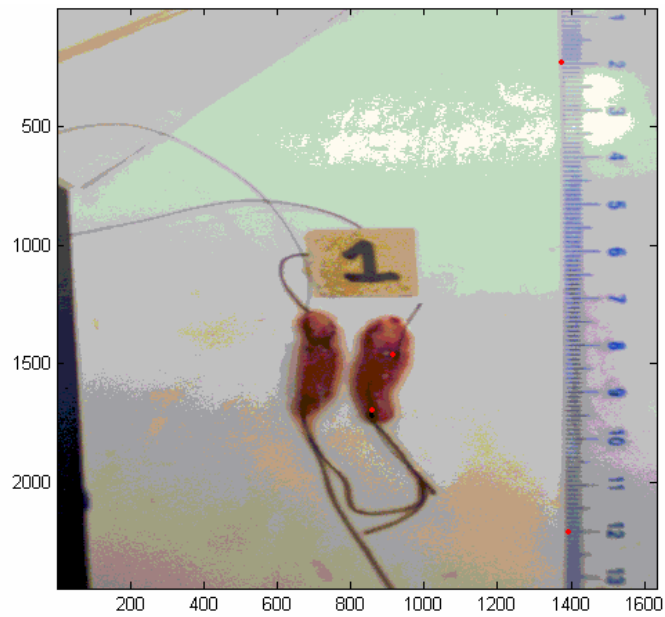


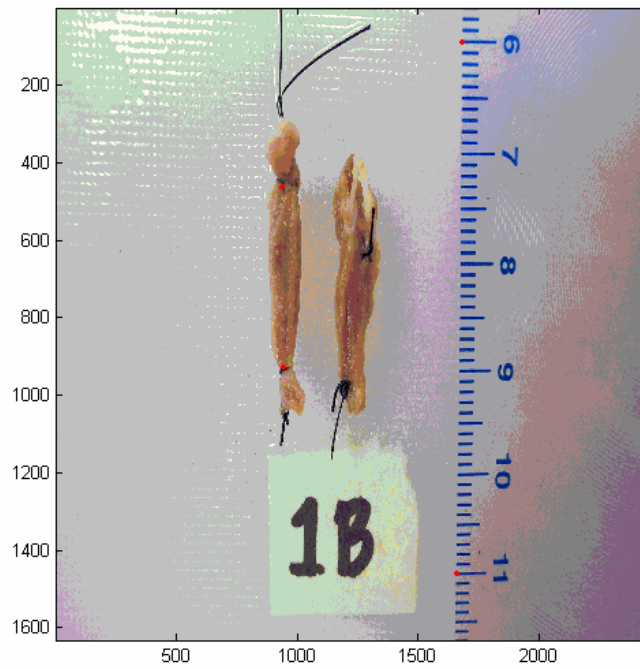Fig. 38. Unstretched septum with marker points on posterior segment (Animal 1).

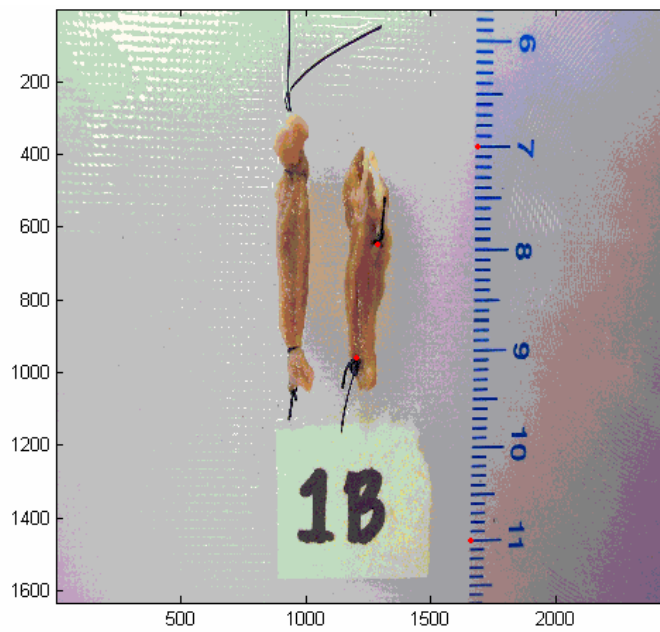Fig. 39. Stretched septum with marker points on anterior segment (Animal 1).



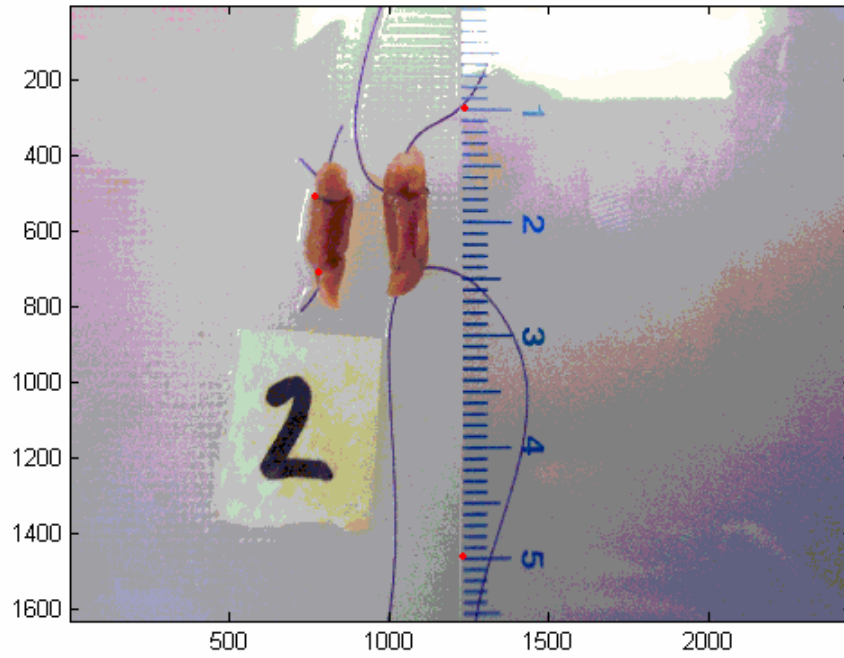Fig. 40. Stretched septum with marker points on posterior segment (Animal 1).

Fig. 41. Unstretched septum with marker points on anterior segment (Animal 2).
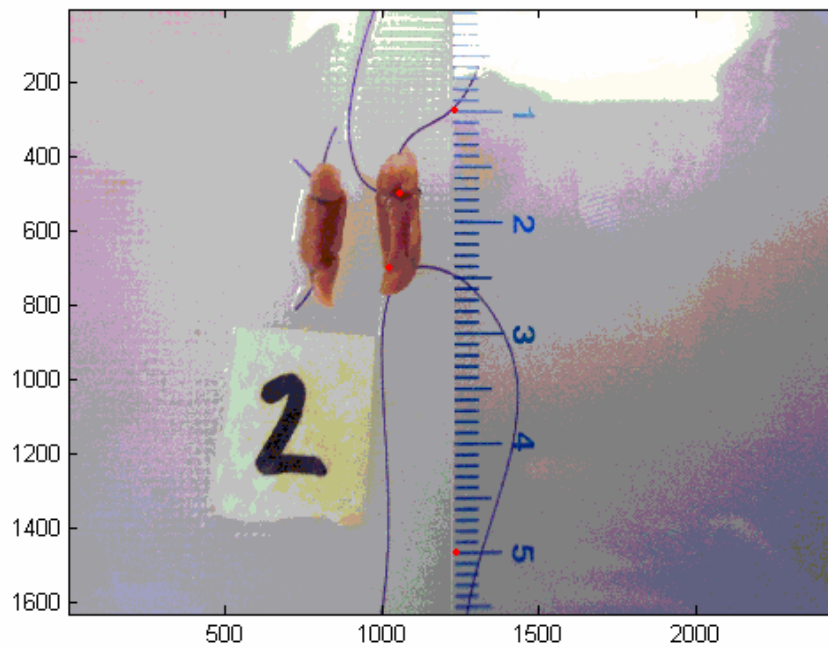


Fig. 42. Unstretched septum with marker points on posterior segment (Animal 2).
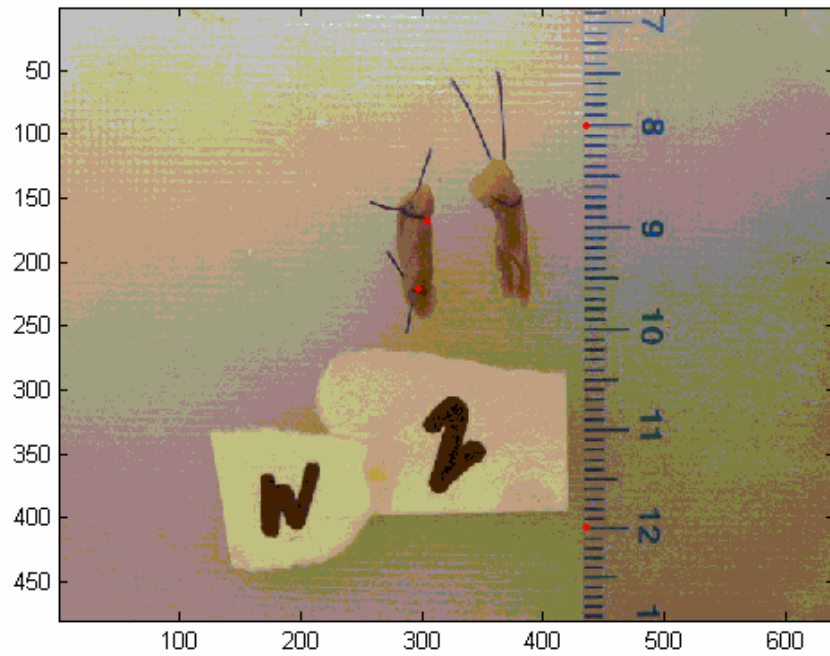
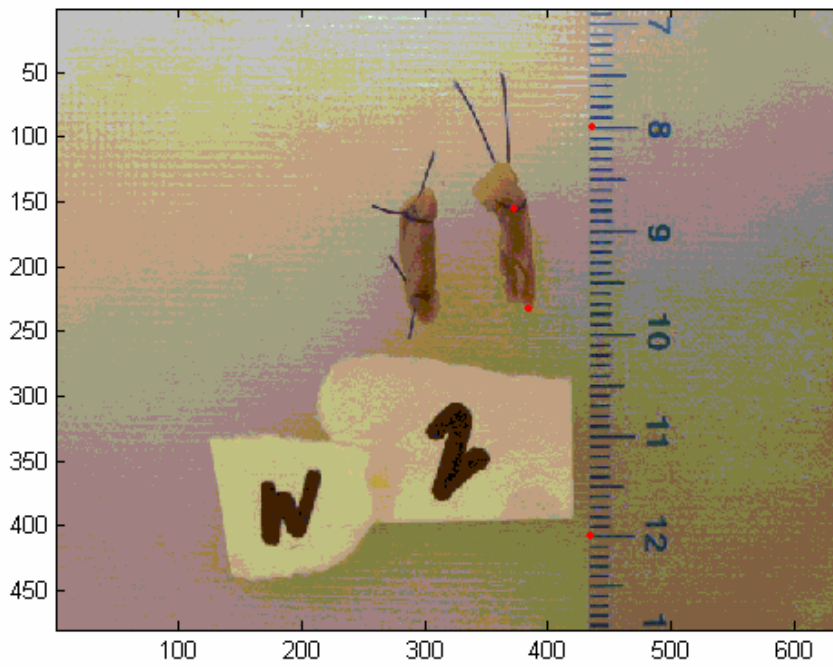Fig. 43. Stretched septum with marker points on anterior segment (Animal 2).


Fig. 44. Stretched septum with marker points on posterior segment (Animal 2).

# VITA

Name:                       Kristina Diane Aghassibake

Permanent Address:   605 San Juan Court
                              Irving, TX 75062

Date of Birth:           July 13, 1982

Education:                Texas A&M University
                              College Station, TX 77843
                              Bachelor of Science, Biomedical Engineering, 2002

                              Texas A&M University
                              College Station, TX 77843
                              Master of Science, Biomedical Engineering, 2004